

# Gauss-Bonnet Inflation after Planck2018

Narges Rashidi<sup>1</sup> and Kourosh Nozari<sup>2</sup>

Department of Theoretical Physics, Faculty of Basic Sciences, University of Mazandaran,  
P. O. Box 47416-95447, Babolsar, IRAN  
Research Institute for Astronomy and Astrophysics of Maragha (RIAAM),  
P. O. Box 55134-441, Maragha, Iran

## Abstract

We study the primordial perturbations and reheating process in the models where the Gauss-Bonnet term is non-minimally coupled to the canonical and non-canonical (DBI and tachyon) scalar fields. We consider several potentials and Gauss-Bonnet coupling terms as power-law, dilaton-like, cosh-type, E-model and T-model. To seek the observational viability of these models, we study the scalar perturbations numerically and compare the results with the Planck2018 TT, TE, EE+lowE+lensing+BK14+BAO joint data at 68% CL and 95% CL. We also study the tensor perturbations in confrontation with the Planck2018 TT, TE, EE+lowE+lensing+BK14+BAO+ LIGO&Virgo2016 joint data at 68% CL and 95% CL. In this regard, we obtain some constraints on the Gauss-Bonnet coupling parameter  $\beta$ . Another important process in the early universe is the reheating phase after inflation which is necessary to reheat the universe for subsequent evolution. In this regard, we study the reheating process in these models and find some expressions for the e-folds number and temperature during that era. Considering that from Planck TT,TE,EE+lowEB+lensing data and BICEP2/Keck Array 2014, based on the  $\Lambda$ CDM+ $r + \frac{dn_s}{d \ln k}$  model, we have  $n_s = 0.9658 \pm 0.0038$  and  $r < 0.072$ , we obtain some constraints on the e-folds number and temperature. From the values of the e-folds number and the effective equation of state and also the observationally viable value of the scalar spectral index, we explore the capability of the models in explaining the reheating phase.

**PACS:** 98.80.Bp, 98.80.Cq, 98.80.Es

**Key Words:** Cosmological Inflation, Gauss-Bonnet Effect, Primordial Perturbation, Reheating Process, Observational Constraints.

---

<sup>1</sup>n.rashidi@umz.ac.ir

<sup>2</sup>knozari@umz.ac.ir

# 1 Introduction

One simplest way to solve some problems of the standard model of cosmology is to consider a single canonical scalar field (inflaton) with a flat potential leading to the slow-roll of the inflaton. The slow-rolling of the inflaton causes enough exponential expansion of the early universe. The primordial perturbations in this single field model would have an adiabatic, scale invariant and gaussian dominant modes [1, 2, 3, 4, 5, 6, 7, 8, 9]. However, some cosmologists are interested in the extended inflation models predicting the non-Gaussian distributed perturbations [9, 10, 11, 12, 13, 14, 15, 16, 17].

Thinking over the very early time in the history of the universe, approaching the Planck scale, and studying that epoch, it seems necessary to incorporate some quantum corrections into the Einstein gravity. The quantum theory of gravity at the low-energy limit leads to the Einstein theory of gravity [18]. There is this belief that, as a promising candidate for the quantum gravity, we can consider the string theory. To import the quantum effects of gravity by using the higher-order curvature correction to the gravitational action, the string theory suggests to consider the Gauss-Bonnet (GB) term [19]. This term is a quadratic term defined by

$$\mathcal{L}_{GB} = R_{abcd} R^{abcd} - 4R_{ab} R^{ab} + R^2 \quad (1)$$

which is part of Lovelock's theorem [20] and its role in the dynamics of the early universe is significant [21, 22]. By adding this term to the action of the theory, which makes the action ghost-free, we don't face the unitarity problem. However, it turns out that, when we deal with the GB term in dimensions less than five, this term behaves just like a topological term and therefore has no influence on the background dynamics. To import the GB effect on the background dynamics, one way is to consider the GB term in higher dimensions [23, 24, 25, 26, 27, 28, 29]. Another way, if we look for the GB effect in 4 dimensions, is to couple it non-minimally to a scalar field or adopt a function of GB term in the 4-dimensional action [30, 31, 32, 33, 34, 35, 36, 37, 38, 39, 40, 41]. Among the works done on this issue, we focus on the models in which the GB term is non-minimally coupled to the scalar field in the theory. Some authors have studied this type of GB inflation models and found some interesting observational results. In this regard, the Gauss-Bonnet inflation models with power-law, inverse power-law and exponential potentials and GB coupling have been studied [33, 34, 35, 39, 42] and the results have been compared with different data sets such as WMAP 5-year [43], Planck+WP [44], Planck+WP+highL+BICEP2 [45] and BICEP2/Keck-Array [46] data.

Another interesting case in studying the inflation models is the idea of “cosmological attractor”. In this regard,  $\alpha$ -attractor models are one class of the models incorporating the idea of cosmological attractors which have attracted a lot of attention [47, 48, 49, 50, 51, 52, 53, 54, 55, 56, 57, 58, 59, 60]. In the  $\alpha$ -attractor models, the E-model potential is given by  $V \sim \left[1 - \exp\left(-\sqrt{\frac{2\kappa^2}{3\alpha}}\phi\right)\right]^{2n}$ . It is interesting to consider the GB coupling term as E-model and study the inflation and perturbations [61, 62]. T-Model potential in the  $\alpha$ -attractor models is given by  $V \sim \tanh^{2n}\left(\frac{\kappa\phi}{\sqrt{6\alpha}}\right)$ . It is also possible to take the GB term in the inflation models as T-model, which gives cosmologically viable results [62].

On the other hand, we should notice that the scalar field responsible for the inflation can be a canonical as well as a non-canonical scalar field like as tachyon [65, 66, 67] or Dirac-Born-Infeld (DBI) [63, 64]. Studying the inflation in tachyon and DBI models

gives interesting results [14, 68, 69, 70, 71, 72, 73, 74, 75]. In this regard, one can consider the coupling between these non-canonical scalar fields and the GB term. Also, it is possible in the GB inflation models to consider the nonminimal coupling or nonminimal derivative coupling between the scalar field and gravity (or any generalized inflationary models) [76, 77].

Although a lot of works have been done on the GB inflation issue, the observational viability of those models depends on the newest data released at any time. Recently, the Planck 2018 collaboration have released the new results [78, 79]. From Planck2018 TT,TE,EE+lowE+lensing data<sup>1</sup>, based on the  $\Lambda$ CDM+ $r+\frac{dn_s}{d\ln k}$  model which supports quasi-de Sitter expansion of the universe during inflation epoch, we have constraints on the scalar spectral index and tensor-to-scalar ratio as  $n_s = 0.9647 \pm 0.0044$  and  $r < 0.16$  [78]. However, when we consider the joint data of Planck 2018, BAO and BICEP2/Keck Array 2014, that means Planck2018 TT,TE,EE+lowE+lensing+BAO+BK14 data (hereafter, base data), we have  $n_s = 0.9658 \pm 0.0038$  and  $r < 0.072$  [78]. By these new constraints on the perturbation's parameters, some inflation models might be ruled out and the constraints on some parameters of the other inflation models might be changed. Another information that Planck2018 team gives us is on the tensor spectral index. Planck2018 gives the constraint on the tensor spectral index as  $-0.62 < n_T < 0.53$  with  $r < 0.080$ , obtained from Planck2018 TT, TE, EE +lowE+lensing+BK14+ BAO+LIGO&Virgo2016 joint data (hereafter, base+GW data) [78]. It seems that, analyzing and studying the tensor part of the perturbations in the Gauss-Bonnet models, which has been less studied before, give us some more information about the inflation models.

Another important issue in studying the inflation models is the reheating process after inflation. As long as the potential is sufficiently flat, meaning that the slow-roll parameters  $\epsilon$  and  $\eta$  are very small, the universe inflates exponentially. When one of the slow-roll parameters meets unity, the inflation ends and the inflaton field rolls down to the minimum of the potential. By reaching the minimum of the potential, inflaton starts oscillating about that minimum and losing the energy. In this regard, according to the physics of particles creation and non-equilibrium phenomena, it decays into the plasma of the relativistic particles and the universe becomes radiation-dominated [80, 81, 82]. There are other interesting but complicated reheating scenarios including the non-perturbative processes, proposed by some authors. Some examples of the non-perturbative reheating scenarios are as the parametric resonance decay [83, 84, 85], tachyonic instability [86, 87, 88, 89, 90, 91] and the instant preheating

[92]. To analyze the reheating process, we focus on two important parameters  $N_{rh}$  (e-folds number) and  $T_{rh}$  (temperature) in this phase. Studying these parameters, gives us some more constraints on the model's parameters space [93, 94, 95, 96, 97]. The effective equation of state parameter,  $\omega_{eff}$ , is another important parameter in exploring the reheating phase. For a massive inflaton, domination of the potential over the kinetic energy leads to  $\omega_{eff} = -1$  and domination of the kinetic energy over the potential leads to  $\omega_{eff} = 1$ . Given that at the initial epoch of the reheating process, the massive inflaton oscillates with frequency very larger than the expansion rate, the averaged effective pressure at that epoch is zero. This means that, at the initial epoch of the reheating phase, we can

---

<sup>1</sup>TT, TE and EE refer to temperature auto-power spectrum, temperature-E-mode cross-power spectrum and E-mode polarization auto-power spectrum, respectively. Planck2018 TT,TE,EE+lowEB denotes the combination of the likelihood at multipole  $l \geq 30$  using TT, TE, and EE spectra, the low- $l$  SimAll EE likelihood and the low- $l$  temperature Commander likelihood [78]. When Planck2018 B-mode information is included, the abbreviation is Planck TT,TE,EE+lowEB. Also, BK14 refers to BICEP2/Keck Array 2014 data and BAO denotes Baryon Acoustic Oscillations.

assume  $\omega_{eff} = 0$  which corresponds to the equation of state parameter of the dust matter. Also, at the end of the reheating phase, we have  $\omega_{eff} = \frac{1}{3}$ . Therefore, exploring the effective equation of state gives us some more information about the reheating phase.

Based on these preliminaries, in this paper we focus on the GB inflation models and re-consider them to seek for their observational viability in confrontation with base and base+GW data sets. In this regard, in section 2, we study the inflation and perturbations in the general Gauss-Bonnet model. In section 3, we consider the Gauss-Bonnet model with a canonical scalar field. In this respect, by adopting power-law potential and two types of GB coupling as inverse power-law and dilaton-like couplings, we obtain the tensor-to-scalar ratio, scalar and tensor spectral indices and investigate the observational viability of the model. In section 4, we perform analysis on the the Gauss-Bonnet natural inflation, in which the potential of the scalar field is cos-type and the GB coupling is inverse of cos. The Gauss-Bonnet  $\alpha$ -attractor is studied in section 5, with both E-Model and T-Model potential and GB coupling. In section 6, we analyze a Gauss-Bonnet inflation in which the inflaton is tachyon field. By adopting power-law potential and both inverse power-law and dilaton-like GB coupling, we check the observational viability of this model. The DBI Gauss-Bonnet inflation, with power-law potential, inverse power-law DBI field and both inverse power-law and dilaton-like GB coupling, is explored in section 7. The reheating process after inflation for the GB model with canonical scalar field is investigated in section 8. In this regard, we obtain some expressions for the e-folds number and temperature during reheating process. By using the observational constraint on the scalar spectral index, we find some constraints on  $N_{rh}$  and  $T_{rh}$ . We also study the effective equation of state during this process. In section 9, we investigate the reheating phase in the GB model with tachyon field. The reheating phase in DBI GB model is studied in section 10. In section 11, we present a summary of the paper. We emphasize that, although the GB inflation models have been studied in several papers, however, the tensor perturbations in the GB models have been less studied. Also, the reheating phase is an interesting issue in studying the inflation models, which for most of models we study here, have never been studied.

## 2 The general Gauss-Bonnet Inflation

In this section, we present the inflation and perturbations in a cosmological model in which a Gauss-Bonnet term is non-minimally coupled to the scalar field. In this setup, the action is given by

$$S = \int d^4x \sqrt{-g} \left[ \frac{1}{2\kappa^2} R + P(X, \phi) - \mathcal{G}(\phi) \mathcal{L}_{GB} \right], \quad (2)$$

where  $\phi$  is the scalar field,  $R$  is the Ricci scalar,  $\mathcal{L}_{GB}$  is the Gauss-Bonnet term with the coupling function  $\mathcal{G}(\phi)$ , and  $X = -\frac{1}{2}g^{\mu\nu}\partial_\mu\phi\partial_\nu\phi$ . Action (2) in a spatially flat FRW metric, gives the following background equations

$$H^2 = \frac{\kappa^2}{3\mathcal{F}} \left[ -P + 2XP_{,X} + 24H^3\dot{\mathcal{G}} \right], \quad (3)$$

$$\left( P_X + 2XP_{,XX} \right) \ddot{\phi} + \left( 3HP_{,X} + \dot{\phi}P_{,\phi X} \right) \dot{\phi} - P_{,\phi} + 24H^4\mathcal{G}' + 24H^2\dot{H}\mathcal{G}' = 0, \quad (4)$$

where the subscript “,” shows derivative with respect to the corresponding parameter, a dot denotes a derivative with respect to the cosmic time and a prime shows a derivative with respect to the scalar field.

The slow-roll parameters  $\epsilon$  and  $\eta$ , defined as

$$\epsilon = -\frac{\dot{H}}{H^2}, \quad \eta = -\frac{1}{H} \frac{\ddot{H}}{\dot{H}}, \quad (5)$$

under the conditions  $\epsilon \ll 1$  and  $|\eta| \ll 1$  show the inflation phase. In this extended setup, with GB correction, the slow-roll limits are as  $\ddot{\phi} \ll |3H\dot{\phi}|$ ,  $\dot{\phi}^2 \ll V(\phi)$ ,  $H\dot{\mathcal{G}} \ll \kappa^{-2}$  and  $P_{,X}X \ll \kappa^{-2}H^2$  (see [34, 77, 98]).

The e-folds number, which is defined as

$$N = \int_{t_{hc}}^{t_f} H dt, \quad (6)$$

in this model and within the slow-roll conditions is given by

$$N = \int_{\phi_{hc}}^{\phi_f} \frac{3H^2 P_{,X}}{P_{,\phi} - 24H^4 \mathcal{G}'} d\phi. \quad (7)$$

In equations (6) and (7) the subscript  $hc$  and  $f$  refer to the horizon crossing of the physical scales and the end of the inflation, respectively.

By using the following Arnowitt-Deser-Misner (ADM) perturbed line element

$$ds^2 = -(1 + 2\mathcal{R})dt^2 + 2a(t)\mathcal{D}_i dt dx^i + a^2(t) [(1 - 2\Phi)\delta_{ij} + 2\Theta_{ij}] dx^i dx^j, \quad (8)$$

we present the cosmological linear perturbation in this setup. In the above perturbed metric,  $\mathcal{D}^i$  is defined as  $\mathcal{D}^i = \delta^{ij}\partial_j \mathcal{D} + v^i$  and the parameters  $\mathcal{R}$  and  $\mathcal{D}$  are 3-scalars. Also,  $v^i$  is a vector that satisfies the condition  $v^i_{,i} = 0$  [99, 100]. In this metric, we have denoted the spatial symmetric and traceless shear 3-tensor by  $\Theta_{ij}$  and the spatial curvature perturbation by  $\Phi$ . To study the scalar perturbation at the linear level, we consider the scalar part of the the perturbed metric within the uniform-field gauge (where,  $\delta\phi = 0$ ), as

$$ds^2 = -(1 + 2\mathcal{R})dt^2 + 2a(t)\mathcal{D}_{,i} dt dx^i + a^2(t)(1 - 2\Phi)\delta_{ij} dx^i dx^j. \quad (9)$$

By using this perturbed metric, the action (2) is expanded up to the second order in perturbations, leading to the following quadratic action

$$S_2 = \int dt d^3x a^3 \mathcal{W}_s \left[ \dot{\Phi}^2 - \frac{c_s^2}{a^2} (\partial\Phi)^2 \right], \quad (10)$$

where

$$\begin{aligned} \mathcal{W}_s = & \left( \frac{1}{\kappa^2} - 8H\dot{\mathcal{G}} \right) \left[ \left( \frac{1}{\kappa^2} - 8H\dot{\mathcal{G}} \right) \left( 3(XP_{,X} + 2X^2 P_{,XX}) + 144H^3 \dot{\mathcal{G}} \right) + 9 \left( \frac{2H}{\kappa^2} - 24H^2 \dot{\mathcal{G}} \right)^2 \right] \\ & \times \left[ 3 \left( \frac{2H}{\kappa^2} - 24H^2 \dot{\mathcal{G}} \right)^2 \right]^{-1}, \end{aligned} \quad (11)$$

and the square of the sound speed is given by

$$c_s^2 = 3 \left[ 2 \left( \frac{1}{\kappa^2} - 8H\dot{\mathcal{G}} \right)^2 \left( \frac{2H}{\kappa^2} - 24H^2\dot{\mathcal{G}} \right) H - \left( \frac{2H}{\kappa^2} - 24H^2\dot{\mathcal{G}} \right)^2 \left( \frac{1}{\kappa^2} - 8\ddot{\mathcal{G}} \right) + 4 \left( \frac{1}{\kappa^2} - 8H\dot{\mathcal{G}} \right) \left( \frac{d}{dt} \left( \frac{1}{\kappa^2} - 8H\dot{\mathcal{G}} \right) \right) \left( \frac{2H}{\kappa^2} - 24H^2\dot{\mathcal{G}} \right) - 2 \left( \frac{1}{\kappa^2} - 8H\dot{\mathcal{G}} \right)^2 \left( \frac{d}{dt} \left( \frac{2H}{\kappa^2} - 24H^2\dot{\mathcal{G}} \right) \right) \right] \left[ \frac{1}{\kappa^2} - 8H\dot{\mathcal{G}} \right] \left[ \left( \frac{1}{\kappa^2} - 8H\dot{\mathcal{G}} \right) \left( 3(XP_{,X} + 2X^2P_{,XX}) - \frac{9}{\kappa^2}H^2 + 144H^3\dot{\mathcal{G}} \right) + 9 \left( \frac{2H}{\kappa^2} - 24H^2\dot{\mathcal{G}} \right)^2 \right]. \quad (12)$$

The following two-point correlation function is used to survey the power spectrum of the curvature perturbation

$$\langle 0 | \Phi(0, \mathbf{k}_1) \Phi(0, \mathbf{k}_2) | 0 \rangle = (2\pi)^3 \delta^3(\mathbf{k}_1 + \mathbf{k}_2) \frac{2\pi^2}{k^3} \mathcal{A}_s, \quad (13)$$

with  $\mathcal{A}_s$ , the power spectrum, defined by

$$\mathcal{A}_s = \frac{H^2}{8\pi^2 \mathcal{W}_s c_s^3}. \quad (14)$$

The scalar spectral index is obtained by using the power spectrum as

$$n_s - 1 = \left. \frac{d \ln \mathcal{A}_s}{d \ln k} \right|_{c_s k = aH}, \quad (15)$$

which is calculated at the time where the physical scales exit of the sound horizon. In this setup the scalar spectral index is obtained as

$$n_s - 1 = -2\epsilon - \frac{\frac{d \left( \epsilon - \frac{4H\dot{\mathcal{G}}}{\kappa^2} \right)}{dt}}{H \left( \epsilon - \frac{4H\dot{\mathcal{G}}}{\kappa^2} \right)} - \frac{1}{H c_s} \frac{d c_s}{dt}. \quad (16)$$

By focusing on the tensor part of the perturbed metric (8), we can explore the tensorial perturbations. In this regard, we write the 3-tensor  $\Theta_{ij}$  as

$$\Theta_{ij} = \Theta_+ \vartheta_{ij}^+ + \Theta_\times \vartheta_{ij}^\times, \quad (17)$$

where  $\vartheta_{ij}^{(+,\times)}$  are two polarization tensors that satisfy the reality and normalization conditions [12, 13]. Now, the quadratic (second order) action for the tensor mode is the following expression

$$S_T = \int dt d^3x a^3 \mathcal{W}_T \left[ \dot{\Theta}_+^2 - \frac{c_T^2}{a^2} (\partial \Theta_+)^2 + \dot{\Theta}_\times^2 - \frac{c_T^2}{a^2} (\partial \Theta_\times)^2 \right]. \quad (18)$$

In this second order action, the parameters  $\mathcal{W}_T$  and  $c_T^2$  are given by

$$\mathcal{W}_T = \frac{1}{4\kappa^2} \left( 1 - 8\kappa^2 H\dot{\mathcal{G}} + \frac{\kappa^2 X \mathcal{N}}{M^2} \right), \quad (19)$$

$$c_T^2 = 1 + 8\kappa^2 H \dot{\mathcal{G}} - \frac{2\kappa^2 X \mathcal{N}}{M^2}. \quad (20)$$

For the tensor mode, the amplitude of the perturbations is defined as

$$\mathcal{A}_T = \frac{H^2}{2\pi^2 \mathcal{W}_T c_T^3}, \quad (21)$$

and the tensor spectral index in this setup is given by

$$n_T = \frac{d \ln \mathcal{A}_T}{d \ln k} = 2\epsilon. \quad (22)$$

Another important perturbation parameter, the tensor-to-scalar ratio, is defined as the ratio of the amplitudes of the tensor mode versus the scalar mode:

$$r = \frac{\mathcal{A}_T}{\mathcal{A}_s} \simeq 16c_s\epsilon = -8c_s(n_T + 8\kappa^2 H \dot{\mathcal{G}}). \quad (23)$$

For more details about obtaining the equations presented in this section, see [12, 76, 77]. By having the required equations, in the next sections we explore the observational viability of some Gauss-Bonnet models.

### 3 Gauss-Bonnet Inflation in a Model with the Canonical Scalar Field

In this section, we consider the case where

$$P(X, \phi) = X - V. \quad (24)$$

This choice of  $P(X, \phi)$  corresponds to the simple inflation model where the inflaton rolls slowly down a nearly flat potential [1, 2, 3]. By this adoption, we have an inflation model in which a Gauss-Bonnet term is non-minimally coupled to the canonical scalar field. In this case, the scalar spectral index takes the following form

$$n_s = 1 - \frac{16\chi V^3 \mathcal{G}'' + 8\chi' V^3 \mathcal{G}' + 3\chi V'' V - 6\chi V'^2 + 3\chi' V V'}{V(8V^2 \alpha' + 3V')}, \quad (25)$$

where

$$\chi = \frac{V'}{\kappa^2 V} + \frac{8\kappa^2}{3} \mathcal{G}' V. \quad (26)$$

The tensor spectral index is given by

$$n_T = -2 \left( \frac{1}{2\kappa^2} \frac{V'^2}{V^2} + \frac{4}{3} \kappa^2 \mathcal{G}' V' \right). \quad (27)$$

Also, we have the following expression for the tensor-to-scalar ratio

$$r = -8 \left( -\frac{8}{3} \mathcal{G}' \chi V - \frac{\chi V'}{V} \right). \quad (28)$$

Note that in obtaining equations (25)-(28), we have used the slow-roll conditions. Now, we have to choose some explicit functions for the potential and GB coupling function. After adopting the functions, we study the model numerically and compare the results with base<sup>2</sup> and base+GW<sup>3</sup> observational data sets.

### 3.1 Power-Law potential and Inverse Power-Law GB Coupling

The model with the monomial potential and inverse monomial GB coupling function has been considered as the simplest primordial inflation model. In the absence of the GB effect, the simple inflation model with  $\phi^2$  and  $\phi^4$  potentials is not consistent with the base data [78]. We wonder whether the presence of GB effect makes the model observationally viable. In this regard, we adopt following potential and GB coupling function

$$V = V_0 \phi^n \quad \& \quad \mathcal{G} = \mathcal{G}_0 \phi^{-n}. \quad (29)$$

By this choice, we find the following expressions for the perturbation parameters

$$n_s = 1 - \frac{(n+2)(2\beta-1)n}{\phi^2}, \quad (30)$$

$$n_T = \frac{n^2(\beta-1)}{\phi^2}, \quad (31)$$

and

$$r = 8 \frac{n^2(\beta-1)^2}{\phi^2}, \quad (32)$$

where

$$\beta = \frac{8}{3} V_0 \mathcal{G}_0, \quad (33)$$

and we have set  $\kappa^2 \equiv 1$ . We can use equation (7) to obtain the value of the scalar field at the time of the horizon crossing of the physical scales. Now, we perform a numerical analysis on the model's parameter space. In this regard, we explore  $r - n_s$  and  $r - n_t$  in confrontation with Planck2018 different data sets. To study  $r - n_s$  behavior, we use the base data. Note that, from this data set we have  $n_s = 0.9658 \pm 0.0038$  and  $r < 0.072$ , based on the  $\Lambda\text{CDM}+r + \frac{dn_s}{d\ln k}$  model. These constraints on the perturbation parameters imply the constraints  $52.13 \leq N \leq 65.29$  and  $0.407 \leq \mathcal{G} \leq 0.528$  on the GB model with  $V = V_0 \phi^n$  and  $\mathcal{G} = \mathcal{G}_0 \phi^{-n}$  and for  $n = 2$ . In the top panels of Figure 1, we see  $r - n_s$  plane in the background of the base data. In plotting this figure (and all subsequent figures of this type), we have used  $n = 2, 4$ ,  $50 \leq N \leq 70$  and also  $0 < \beta < 1$ . As figure shows,  $r - n_s$  plane in the GB model with  $n = 2$ , in some ranges of the parameters space is consistent with the observational data. However, for  $n = 4$ , there is no consistency of  $r - n_s$  plane with the base data.

In the sense that in studying the tensor spectral index we focus on the tensor part of the perturbations (the gravitational waves), we use the base+GW data to explore  $r - n_T$ . The results are shown in the bottom panels of Figure 1. In this case, the  $r - n_T$  plane for both  $n = 2$  and  $n = 4$

<sup>2</sup> Planck2018 TT,TE,EE+lowE+lensing+BAO +BK14

<sup>3</sup> Planck2018 TT, TE, EE +lowE+lensing+BK14+ BAO+LIGO&Virgo2016



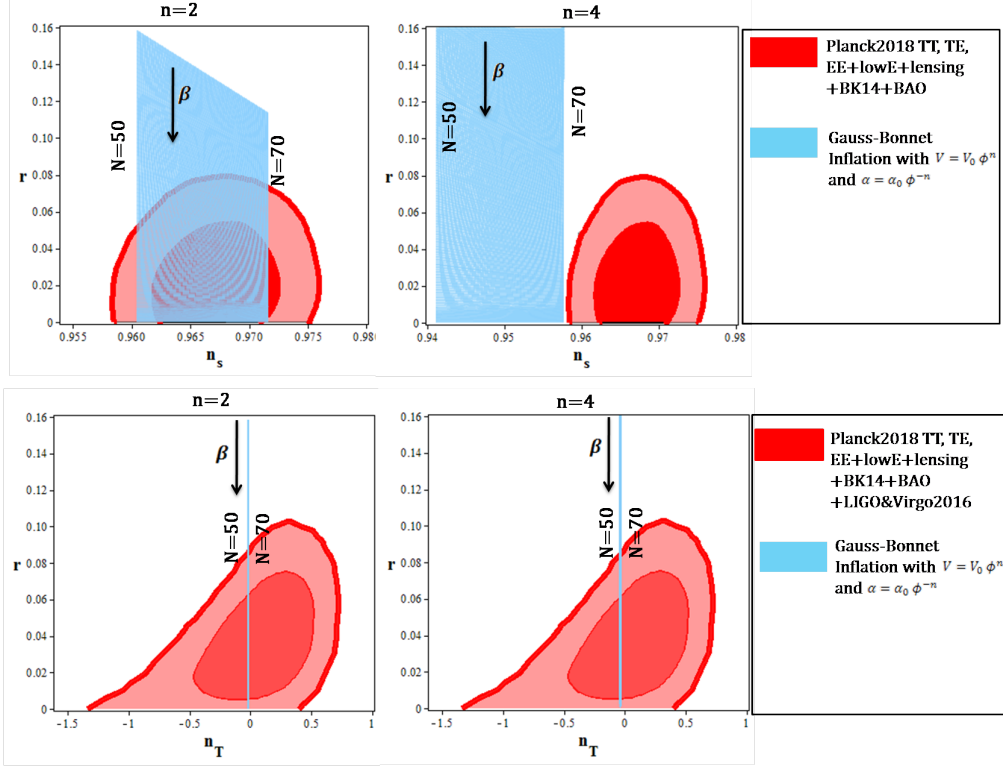


Figure 1: Tensor-to-scalar ratio versus the scalar spectral index and tensor spectral index of the GB model with  $V = V_0 \phi^n$  and  $\mathcal{G} = \mathcal{G}_0 \phi^{-n}$ .

is consistent with the base+GW data. By numerical analysis of the model in this case, we have obtained some constraints on the model's parameter space which are presented in Table 1. Note that, in [78] it has been used the 68% CL on measured parameter ( $n_s$ ) and 95% CL for top bound on other parameters ( $r$  and  $n_T$ ). In this respect, and as regards we study these three parameters to obtain the constraints, both confidence levels are interesting to consider.

In summary, our numerical analysis shows that the Gauss-Bonnet inflation with  $V = V_0 \phi^n$  and  $\mathcal{G} = \mathcal{G}_0 \phi^{-n}$  for  $n = 2$  is consistent with observational data if  $\beta \sim \mathcal{O}(10^{-1})$ . Also, this model with  $V = V_0 \phi^n$  and  $\mathcal{G} = \mathcal{G}_0 \phi^{-n}$  for  $n = 4$  is ruled out. Note that, as it can be seen from Table 1, any small variation of the parameter  $\beta$  can cause the model not to be consistent with the observational data. This means that, physically, not only the presence of the Gauss-Bonnet term but also the intensity of the coupling between the Gauss-bonnet term (as the geometry side of the model) and the scalar field (as the energy-momentum side of the model) is very important in the viability of the model.

### 3.2 Power-Law Potential and Dilaton-Like GB Coupling

Inspired from heterotic string theory, the GB term appears to be coupled to the dynamical dilaton field with an exponential coupling function. This issue has been studied in Ref. [24]. Therefore, in

Table 1: The ranges of the parameter  $\beta$  in which tensor-to-scalar ratio, the scalar spectral index and the tensor spectral index of the the GB model with  $V = V_0 \phi^n$  and  $\mathcal{G} = \mathcal{G}_0 \phi^{-n}$  are consistent with different data sets.

Planck2018 TT,TE,EE+lowE +lensing+BK14+BAO		Planck2018 TT,TE,EE+lowE +lensing+BK14+BAO		Planck2018 TT,TE,EE+lowE lensing+BK14+BAO +LIGO&Virgo2016		Planck2018 TT,TE,EE+lowE lensing+BK14+BAO LIGO&Virgo2016	
$N$	68% CL		95% CL		68% CL		95% CL
$n = 2$	50	not consistent		$0.680 \leq \beta < 1$		$0.610 \leq \beta \leq 0.970$	$0.470 \leq \beta < 1$
	60	$0.601 \leq \beta < 1$		$0.410 \leq \beta < 1$		$0.520 \leq \beta \leq 0.964$	$0.340 \leq \beta < 1$
	70	$0.660 \leq \beta < 1$		$0.350 \leq \beta < 1$		$0.450 \leq \beta \leq 0.960$	$0.260 \leq \beta < 1$
$n = 4$	50	not consistent		not consistent		$0.810 \leq \beta \leq 0.985$	$0.730 \leq \beta < 1$
	60	not consistent		not consistent		$0.770 \leq \beta \leq 0.982$	$0.680 \leq \beta < 1$
	70	not consistent		not consistent		$0.730 \leq \beta \leq 0.980$	$0.630 \leq \beta < 1$

this subsection, we adopt following potential and GB coupling function

$$V = V_0 \phi^n \quad \& \quad \mathcal{G} = \mathcal{G}_0 e^{-\lambda \phi}. \quad (34)$$

In this case, we have the perturbation parameters of the model as

$$n_s = 1 - \frac{-n(n+2) + \beta \lambda e^{-\lambda \phi} \phi^{n+1} (2\lambda \phi - n)}{\phi^2}, \quad (35)$$

$$n_T = -\frac{n(n - \beta \lambda e^{-\lambda \phi} \phi^{n+1})}{\phi^2}, \quad (36)$$

and

$$r = \frac{8(n - \beta \lambda e^{-\lambda \phi} \phi^{n+1})^2}{\phi^2}. \quad (37)$$

Here also, we use equation (7) to obtain the value of the scalar field at the time of the horizon crossing of the physical scales and then study  $r - n_s$  and  $r - n_T$  behaviors. top panels of Figure 2 show  $r - n_s$  plane in the background of the base data for  $N = 60$ . As figure shows,  $r - n_s$  plane in the GB model with both  $n = 2$  and  $n = 4$ , in some ranges of the parameters  $\lambda$  and  $\beta$  is consistent with the observational data.

In the bottom panels of Figure 2, we see  $r - n_T$  plane in the background of the base+GW data. Considering that the scalar spectral index, tensor spectral index and the tensor-to-scalar ratio depend on both  $\lambda$  and  $\beta$ , to obtain the observational constraints, we fix  $\lambda$  in some sample values and obtain the observationally viable ranges of  $\beta$ . The results are shown in Table 2. In fact, according to our numerical analysis, the Gauss-Bonnet inflation with  $V = V_0 \phi^n$  and  $\mathcal{G} = \mathcal{G}_0 e^{-\lambda \phi}$  for  $n = 2$  is consistent with observational data if  $\beta \gtrsim \mathcal{O}(10^{-2})$ . Also, this model for  $n = 4$  is consistent with observational data if  $\beta \sim \mathcal{O}(10^{-1})$ .

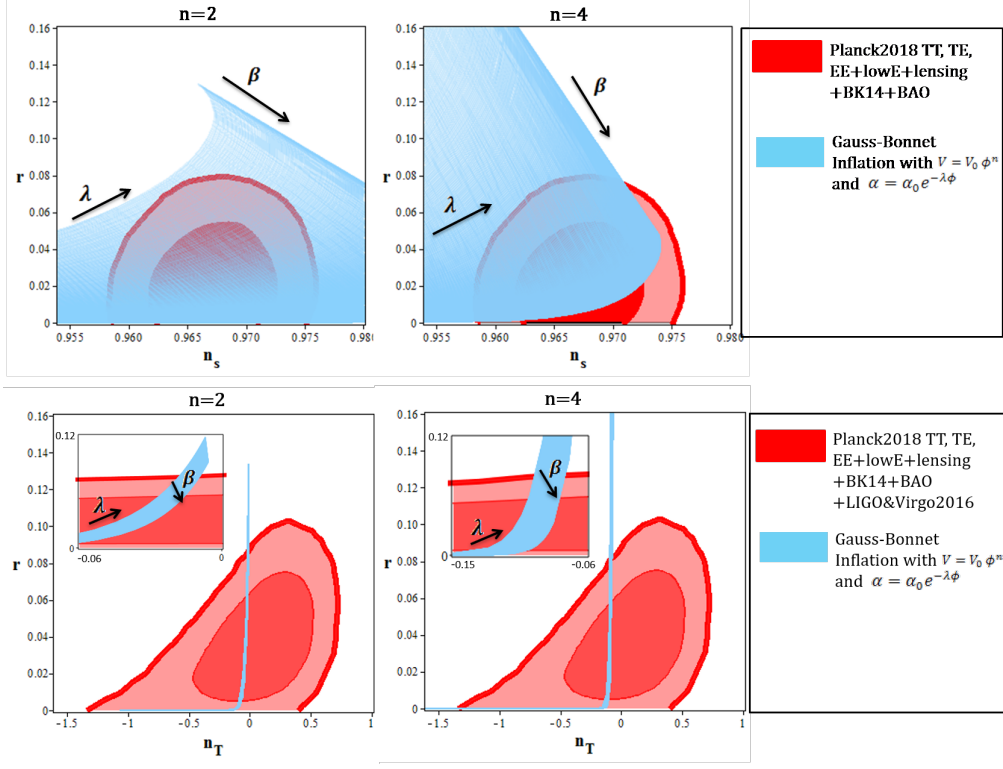


Figure 2: Tensor-to-scalar ratio versus the scalar spectral index and tensor spectral index of the GB model with  $V = V_0 \phi^n$  and  $\mathcal{G} = \mathcal{G}_0 e^{-\lambda\phi}$ .

Table 2: The ranges of the parameter  $\beta$  in which the tensor-to-scalar ratio, the scalar spectral index and the tensor spectral index of the the GB model with  $V = V_0 \phi^n$  and  $\mathcal{G} = \mathcal{G}_0 e^{-\lambda\phi}$  are consistent with different data sets.

		Planck2018 TT,TE,EE+lowE +lensing+BK14+BAO	Planck2018 TT,TE,EE+lowE +lensing+BK14+BAO	Planck2018 TT,TE,EE+lowE lensing+BK14+BAO +LIGO&Virgo2016	Planck2018 TT,TE,EE+lowE lensing+BK14+BAO LIGO&Virgo2016
$N$		68% CL	95% CL	68% CL	95% CL
$n = 2$	10	$0.03 \leq \beta \leq 0.05$	$0.01 \leq \beta \leq 0.072$	$0.01 \leq \beta \leq 0.121$	$0.002 \leq \beta < 1$
	$10^2$	$0.062 \leq \beta \leq 0.084$	$0.016 \leq \beta \leq 0.095$	$0.031 \leq \beta \leq 0.184$	$0.020 \leq \beta < 1$
	$10^4$	$0.041 \leq \beta \leq 0.180$	$0.031 \leq \beta \leq 0.420$	$0.086 \leq \beta \leq 0.269$	$0.260 \leq \beta < 1$
$n = 4$	10	$0.610 \leq \beta \leq 0.683$	$0.580 \leq \beta \leq 0.716$	$0.435 \leq \beta \leq 0.812$	$0.016 \leq \beta \leq 0.871$
	$10^2$	$0.642 \leq \beta \leq 0.711$	$0.621 \leq \beta \leq 0.743$	$0.483 \leq \beta \leq 0.865$	$0.033 \leq \beta \leq 0.895$
	$10^4$	$0.693 \leq \beta \leq 0.789$	$0.670 \leq \beta \leq 0.826$	$0.506 \leq \beta \leq 0.884$	$0.081 \leq \beta \leq 0.910$

## 4 GB Natural Inflation

In the inflation models, to fit with the CMB anisotropy measurements, there should be a large number of e-folds of the scale factor. This means that the width of the potential in the inflation models must be much larger than its height. In this respect, the authors of Ref. [101] have shown that, in order to the potential be flat, the ratio between the height and the fourth power of the width must satisfy the constraint  $\Delta V/(\Delta\phi)^4 \leq 10^{-6}$ . In this constraint,  $\Delta$  refers to the change in the corresponding parameters. In this regard, in 1990, Freese, Frieman, and Olinto have proposed the natural inflation model [102]. In their model, they have considered an axion-like particle (a pseudo-Nambu-Goldstone boson) as the field responsible for the primordial inflation. Invariance of the potential under a transformation as  $\phi \rightarrow \phi + \text{constant}$  (a shift symmetry) ensures flatness of the potential [102, 103]. The symmetry is broken after enough inflation and the inflation phase terminates. Based on these preliminaries, we consider a GB model where the potential is the natural potential type and the GB coupling is inverse of the natural potential as

$$V = V_0 \left[ 1 + \cos \left( \frac{\phi}{f} \right) \right] \quad \& \quad \mathcal{G} = \mathcal{G}_0 \left[ 1 + \cos \left( \frac{\phi}{f} \right) \right]^{-1}. \quad (38)$$

Note that, the natural inflation in its simplest realization, has the above form of the potential. By these functions, the perturbation parameters take the following forms

$$n_s = 1 - \frac{\left( \cos \left( \frac{\phi}{f} \right) - 3 \right) (1 - \beta)}{f^2 \left( 1 + \cos \left( \frac{\phi}{f} \right) \right)}, \quad (39)$$

$$n_T = - \frac{\left( -1 + \beta \right) \left( \cos \left( \frac{\phi}{f} \right) - 1 \right)}{f^2 \left( 1 + \cos \left( \frac{\phi}{f} \right) \right)}, \quad (40)$$

$$r = \frac{8 \left( -1 + \beta \right)^2 \left( 1 - \cos \left( \frac{\phi}{f} \right) \right)}{f^2 \left( 1 + \cos \left( \frac{\phi}{f} \right) \right)}. \quad (41)$$

By using equation (7), to obtain the value of the scalar field at horizon crossing, and equations (39)-(41), we can study the model numerically. To this end, we adopt  $N = 60$  and explore  $r - n_s$  and  $r - n_T$  planes for various values of  $f$  and  $\beta$ . The top panel of Figure 3 shows the tensor-to-scalar ratio versus the scalar spectral index in the background of the base data. As Figure 3 shows, the natural GB inflation in some ranges of the parameter space is observationally viable.

Tensor-to-scalar ratio versus the tensor spectral index in the background of the base+GW data is shown in the bottom panel of Figure 3. By performing a numerical analysis, we have found some constraints on the model's parameters which have been summarized in Table 3. Note that, the natural inflation with  $N = 50$  is not consistent with new observational data. However, when we consider the GB effect, this model for  $\beta \geq 0.65$  is consistent with base and base+GW data sets.

## 5 Gauss-Bonnet $\alpha$ -attractor

In recent years, the idea of the ‘‘cosmological attractor’’ has attracted **the attention of some cosmologists**. Among the models that incorporate the idea of cosmological attractors, we mention

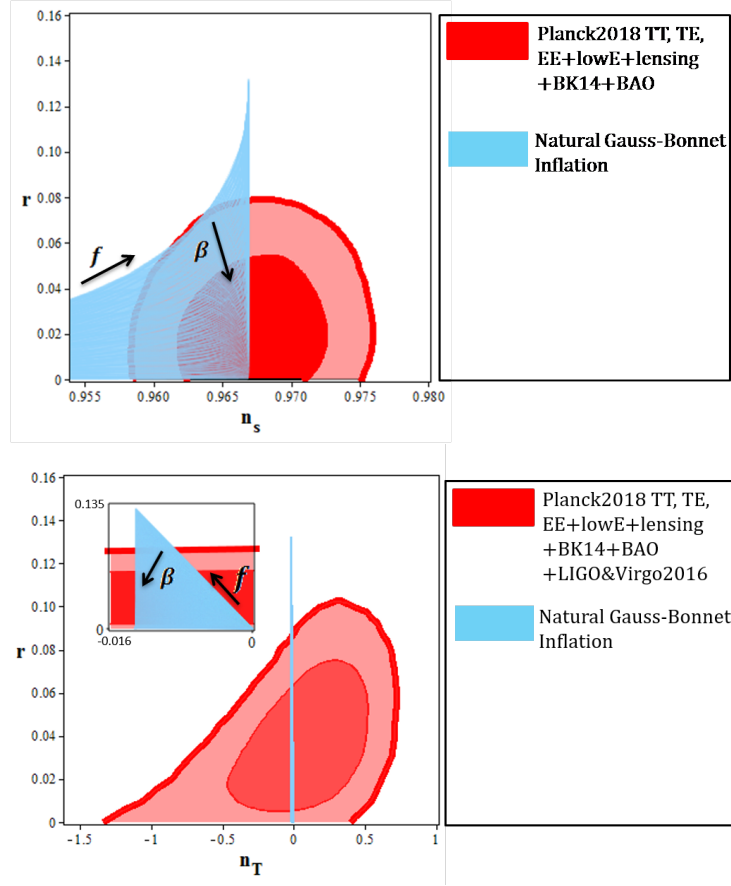


Figure 3: Tensor-to-scalar ratio versus the scalar spectral index and tensor spectral index of the GB natural inflation.

Table 3: The ranges of the parameter  $\beta$  in which the tensor-to-scalar ratio, the scalar spectral index and the tensor spectral index of the GB natural inflation are consistent with different data sets.

	Planck2018 TT,TE,EE+lowE +lensing+BK14+BAO	Planck2018 TT,TE,EE+lowE +lensing+BK14+BAO	Planck2018 TT,TE,EE+lowE lensing+BK14+BAO +LIGO&Virgo2016	Planck2018 TT,TE,EE+lowE lensing+BK14+BAO LIGO&Virgo2016
$N$	68% CL	95% CL	68% CL	95% CL
4	$0.635 \leq \beta < 1$	$0.525 \leq \beta < 1$	$0 \leq \beta \leq 0.962$	all values of $\beta$
15	$0.578 \leq \beta < 1$	$0.345 \leq \beta < 1$	$0.520 \leq \beta \leq 0.962$	$0.341 \leq \beta < 1$
35	$0.596 \leq \beta < 1$	$0.393 \leq \beta < 1$	$0.520 \leq \beta \leq 0.962$	$0.341 \leq \beta < 1$
60	$0.597 \leq \beta < 1$	$0.400 \leq \beta < 1$	$0.524 \leq \beta \leq 0.962$	$0.346 \leq \beta < 1$

the conformal attractor [104, 105] and  $\alpha$ -attractor models [48, 49, 50]. The important characteristic property in the conformal attractor model is that, in the case of large e-folds number, it has the universal prediction for the primordial curvature perturbations and the tensor-to-scalar ratio as  $n_s = 1 - \frac{2}{N}$  and  $r = \frac{12}{N^2}$ . Considering the single field  $\alpha$ -attractor model, the universal predictions for the mentioned parameters are  $n_s = 1 - \frac{2}{N}$  and  $r = \frac{12\alpha}{N^2}$ . In this section, we consider the Gauss-Bonnet effect on the  $\alpha$ -attractor model. We consider Both potentials leading to the  $\alpha$ -attractor: E-model and T-model. We also adopt E-model and T-model GB coupling function and study the inflation in this setup.

### 5.1 E-Model

In Ref. [105], the authors have considered a model with two real scalar fields,  $\varphi$  and  $\psi$ , which are non-minimally coupled to the gravity. They have also considered a potential term as  $V(\varphi, \psi) = \frac{\lambda}{4}\varphi^2(\varphi - \psi)^2$  by which the  $SO(1, 1)$  symmetry has been broken. By using the conformal gauge as  $\psi^2 - \varphi^2 = 6$ , and introducing a canonically normalized field as  $\varphi = \sqrt{6} \cosh \frac{\phi}{\sqrt{6}}$  and  $\psi = \sqrt{6} \sinh \frac{\phi}{\sqrt{6}}$ , they have obtained an exponential-type potential named E-model which we use in this subsection. In this case, we consider the following potential and GB coupling

$$V = V_0 \left[ 1 - \exp \left( - \sqrt{\frac{2\kappa^2}{3\alpha}} \phi \right) \right]^{2n} \quad \& \quad \mathcal{G} = \mathcal{G}_0 \left[ 1 - \exp \left( - \sqrt{\frac{2\kappa^2}{3\alpha}} \phi \right) \right]^{2n}, \quad (42)$$

where the potential  $V$  is an E-model potential. With these functions, we obtain the perturbation parameters from equations (25)-(28). In this case, the scalar spectral index takes the following form

$$n_s = 1 - \frac{8}{9} \frac{nZ \left( 256 \beta^2 Y^{8n} Z n \kappa^4 - 96 \beta^2 Y^{8n} \kappa^4 + 24 \kappa^4 \beta Y^{4n} n Z - 24 \kappa^4 \beta Y^{4n} \right)}{Y^2 \alpha (8 \beta Y^{4n} + 3)} - \frac{8}{9} \frac{nZ \left( 48 \beta Y^{4n} Z n - 36 \beta Y^{4n} - 9 n Z - 9 \right)}{Y^2 \alpha (8 \beta Y^{4n} + 3)}. \quad (43)$$

The tensor spectral index in the E-Model GB inflation is given by

$$n_T = -\frac{8}{9} \frac{n^2 Z^2 (8 \kappa^4 \beta Y^{4n} + 3)}{\alpha Y^2}. \quad (44)$$

Also, we obtain the following expression for the tensor-to-scalar ratio in this case

$$r = \frac{64}{27} \frac{n^2 Z^2 (64 \kappa^4 \beta^2 Y^{8n} + 24 \kappa^4 \beta Y^{4n} + 24 \beta Y^{4n} + 9)}{\alpha Y^2}. \quad (45)$$

In these equations, we have defined the following parameters

$$Y = 1 - Z \quad \text{and} \quad Z = e^{-\frac{\sqrt{6}}{3} \sqrt{\frac{\kappa^2}{\alpha}} \phi}. \quad (46)$$

## 5.2 T-Model

Another interesting case in the  $\alpha$ -attractor model is T-model potential. Authors of Ref. [104] have studied a model with two non-minimally coupled scalar fields and the potential term as  $V(\varphi, \psi) = \frac{1}{36}F(\varphi/\psi)(\varphi^2 - \psi^2)^2$ , which breaks the  $SO(1,1)$  symmetry. Note that  $F(\varphi/\psi)$  is an arbitrary function. By using the gauge and canonically normalized field used in obtaining the E-model potential, they have found the potential as  $V(\phi) = F(\tanh(\phi/\sqrt{6}))$ . In the case of the simplest set of functions as  $F(\varphi/\psi) = \lambda(\varphi/\psi)^{2n}$ , the T-model potential has been obtained. Now, in this subsection, we consider the case where the potential and GB coupling function are T-model type, as

$$V = V_0 \tanh^{2n} \left( \sqrt{\frac{\kappa^2}{6\alpha}} \phi \right), \quad \mathcal{G} = \mathcal{G}_0 \tanh^{2n} \left( \sqrt{\frac{\kappa^2}{6\alpha}} \phi \right). \quad (47)$$

By substituting these potential and GB coupling function in equations (25)-(28), we obtain the scalar spectral index as

$$n_s = 1 + \frac{2}{9} \frac{n \left( 192 \beta^2 \mathcal{U}^{8n} \kappa^4 \mathcal{V} - 256 \beta^2 \mathcal{U}^{8n} n \kappa^4 - 96 \beta \mathcal{U}^{8n} \kappa^4 + 48 \kappa^4 \beta \mathcal{U}^{4n} \mathcal{V} + 9n - 9 \right)}{\mathcal{V}(\mathcal{V} - 1) (8\beta \mathcal{U}^{4n} + 3) \alpha} + \frac{2}{9} \frac{n \left( -24 \kappa^4 \beta \mathcal{U}^{4n} n - 24 \kappa^4 \beta \mathcal{U}^{4n} + 72 \beta \mathcal{U}^{4n} \mathcal{V} - 48 \beta \mathcal{U}^{4n} n - 36 \beta \mathcal{U}^{4n} + 18 \mathcal{V} \right)}{\mathcal{V}(\mathcal{V} - 1) (8\beta \mathcal{U}^{4n} + 3) \alpha}, \quad (48)$$

the tensor spectral index as

$$n_T = -\frac{2}{9} \frac{n^2 (8 \kappa^4 \beta \mathcal{U}^{4n} + 3)}{\alpha \mathcal{V}(\mathcal{V} - 1)}, \quad (49)$$

and finally the tensor-to-scalar ratio as

$$r = \frac{16}{27} \frac{n^2 (64 \kappa^4 \beta^2 \mathcal{U}^{8n} + 24 \kappa^4 \beta \mathcal{U}^{4n} + 24 \beta \mathcal{U}^{4n} + 9)}{\mathcal{V}(\mathcal{V} - 1) \alpha}, \quad (50)$$

where the parameters  $\mathcal{U}$  and  $\mathcal{V}$  are given by

$$\mathcal{U} = \tanh \left( \sqrt{\frac{\kappa^2}{6\alpha}} \phi \right), \quad (51)$$

and

$$\mathcal{V} = \cosh^2 \left( \sqrt{\frac{\kappa^2}{6\alpha}} \phi \right). \quad (52)$$

By substituting the value of the scalar field at horizon crossing in equations (43)-(45) and equations (48)-(50), we can study the GB  $\alpha$ -attractor model numerically. The results are shown in **Figures 7** and **8**. The  $\alpha$ -attractor models with E-model and T-model potential meet the model with  $\phi^n$  potential in  $\alpha \rightarrow \infty$  limit. On the other hand, these models in  $\alpha \rightarrow 0$  and large  $N$  limits reach an attractor point characterized by following scalar spectral index and tensor-to-scalar ratio

$$n_s = 1 - \frac{2}{N}, \quad r = \frac{12\alpha}{N^2}. \quad (53)$$

Table 4: The ranges of the parameter  $\beta$  in which the tensor-to-scalar ratio, the scalar spectral index and the tensor spectral index of the GB  $\alpha$ -attractor model with  $n = 2$  and  $N = 60$  are consistent with different data sets.

	Planck2018 TT,TE,EE+lowE +lensing+BK14+BAO	Planck2018 TT,TE,EE+lowE +lensing+BK14+BAO	Planck2018 TT,TE,EE+lowE lensing+BK14+BAO +LIGO&Virgo2016	Planck2018 TT,TE,EE+lowE lensing+BK14+BAO LIGO&Virgo2016
$N$	68% CL	95% CL	68% CL	95% CL
E-model	20 $\beta \leq 5.17 \times 10^{-2}$	$\beta \leq 5.31 \times 10^{-2}$	$\beta < 3.10 \times 10^{-3}$	all values of $\beta$
	50 $\beta \leq 4.92 \times 10^{-2}$	$\beta \leq 5.04 \times 10^{-2}$	$\beta < 4.52 \times 10^{-3}$	all values of $\beta$
	80 $3.23 \times 10^{-4} \leq \beta \leq 4.56 \times 10^{-2}$	$\beta \leq 4.81 \times 10^{-2}$	$\beta < 8.22 \times 10^{-3}$	all values of $\beta$
T-model	20 $\beta \leq 3.30 \times 10^{-1}$	$\beta \leq 4.01 \times 10^{-1}$	$\beta < 8.11 \times 10^{-3}$	all values of $\beta$
	50 $3.03 \times 10^{-4} \leq \beta \leq 1.42 \times 10^{-1}$	$\beta \leq 9.03 \times 10^{-2}$	$\beta < 9.82 \times 10^{-3}$	all values of $\beta$
	80 $4.28 \times 10^{-4} \leq \beta \leq 1.14 \times 10^{-1}$	$\beta \leq 7.01 \times 10^{-2}$	$2.37 \times 10^{-4} < \beta < 1.43 \times 10^{-2}$	all values of $\beta$

The top panels of Figure 4 show the tensor-to-scalar ratio versus the scalar spectral index of a GB model in the background of the base data, for E-model potential and coupling function (left panel) and T-model potential and coupling function (right panel). The black lines have been plotted to show that the GB  $\alpha$ -attractor model in the small  $\alpha$  limit reaches an attractor (green star) and in the large  $\alpha$  limit meets the GB model with  $\phi^2$  potential and GB coupling (pink stars). This figure has been plotted with  $n = 2$  and  $N = 60$ . As we see from figure, the GB model with  $\phi^2$  potential and GB coupling function is not consistent with the base data. However, when we consider E-model or T-model potential and GB coupling function, it is possible to find some ranges in the parameters space leading to observationally viable values of  $r$  and  $n_s$ . Our analysis on  $r - n_s$  viability shows that E-model GB inflation is consistent with base data 68% CL if  $\alpha < 78$  and at 95% CL if  $\alpha < 4.1 \times 10^2$ . Also, T-model GB inflation has consistency with base data at 68% CL if  $\alpha < 43$  and at 95% CL if  $\alpha < 91$ .

The bottom panels of Figure 4 show the tensor-to-scalar ratio versus the tensor spectral index in the background of base+GW data. By performing a numerical analysis on  $r - n_T$  viability, we find that E-model GB inflation is consistent with base+GW data at 68% CL if  $2.12 < \alpha < 1.6 \times 10^2$  and at 95% CL if  $\alpha < 7.4 \times 10^2$ . Also, in T-model GB inflation we find the constraints  $2.43 < \alpha < 73$  at 68% CL and  $\alpha < 2 \times 10^2$  at 95% CL. However, the values of  $\alpha$  imply some constraints on the GB coupling parameter which have been summarized in Table 4, for some sample values of  $\alpha$ .

By these considerations, we conclude that the Gauss-Bonnet inflation with both E-model and T-model potentials and GB coupling functions is consistent with the observational data if  $\beta \lesssim \mathcal{O}(10^{-3})$ .

## 6 Gauss-Bonnet Inflation in a Model with Tachyon Field

Tachyon field is a scalar field associated with D-branes in string theory [65, 66, 67]. This field, which is described by the Dirac-Born-Infeld action, has interesting cosmological applications. The early time inflation in the history of the Universe might be caused by a slow-rolling tachyon field [106,



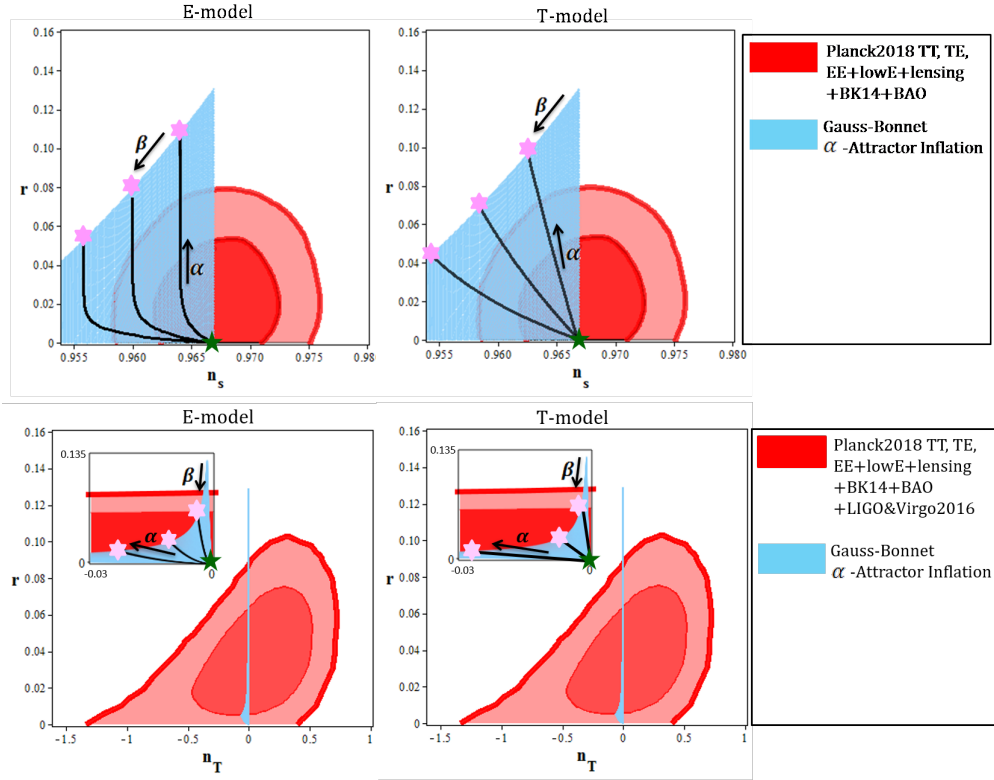


Figure 4: Tensor-to-scalar ratio versus the scalar spectral index and tensor spectral index of the GB  $\alpha$ -attractor. The left panels are corresponding to the case where both potential and GB coupling are E-model. The right panels are corresponding to the case where both potential and GB coupling are T-model. The black lines have been plotted to show that the GB  $\alpha$ -attractor model in the small  $\alpha$  limit reaches an attractor (green star) and in the large  $\alpha$  limit meets the GB model with  $\phi^2$  potential and GB coupling (pink stars).

107, 108]. Also, it is possible that the current acceleration phase of the universe is due to the presence of the tachyon field as the dark energy component [109, 110, 111]. These features make the the tachyon field cosmologically interesting. In the case of tachyon field,  $P(X, \phi)$  is given by the following expression

$$P(X, \phi) = -V\sqrt{1 - 2X}, \quad (54)$$

Now, the scalar spectral index takes the following form

$$n_s = 1 - \frac{16\chi V^3 \mathcal{G}'' + 8\chi' V^3 \mathcal{G}' + 3\chi V'' V - 6\chi V'^2 + 3\chi' V V'}{V(8V^2 \alpha' + 3V')}. \quad (55)$$

The tensor spectral index is given by

$$n_T = -2 \left( \frac{1}{2\kappa^2} \frac{V'^2}{V^2} + \frac{4}{3} \kappa^2 \mathcal{G}' V' \right), \quad (56)$$

and we have the following expression for the tensor-to-scalar ratio

$$r = -8 \left( -\frac{8}{3} \mathcal{G}' \chi V - \frac{\chi V'}{V} \right). \quad (57)$$

In equations (55)-(57), the parameter  $\chi$  is given by

$$\chi = \frac{V'}{\kappa^2 V^2} + \frac{8\kappa^2}{3} \mathcal{G}'. \quad (58)$$

Now, by choosing some explicit functions for the potential and GB coupling, we study this model numerically.

### 6.1 Power-Law potential and Inverse Power-Law GB Coupling

Our first choices for tachyon GB model are the following potential and GB coupling function

$$V = V_0 \phi^n \quad \& \quad \mathcal{G} = \mathcal{G}_0 \phi^{-n}. \quad (59)$$

By these adoptions, we find

$$n_s = 1 - 2 \frac{(2n\beta\kappa^4 + 2\beta\kappa^4 - n - 1)n}{\phi^{n+2}}, \quad (60)$$

$$n_T = -\phi^{-2-n} n^2 (1 - 2\beta), \quad (61)$$

and

$$r = 8 \left[ \phi^{-2-n} n^2 (2\beta - 1)^2 \right]. \quad (62)$$

To compare the model with observational data, we substitute the value of the scalar field at the time of the horizon crossing of the physical scales in the above equations. Then, we perform the numerical analysis on the parameters. In the top panels of Figure 5, we see  $r - n_s$  plane in the background of the base data for  $50 \leq N \leq 70$ . As figure shows, including the GB effect makes

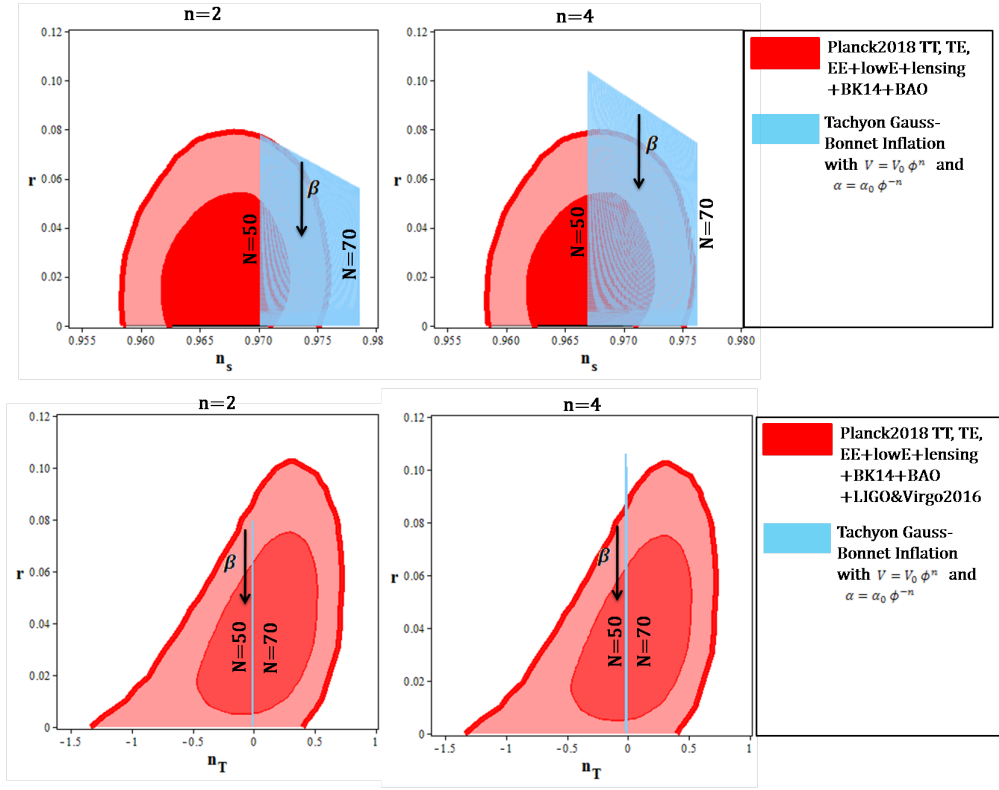


Figure 5: Tensor-to-scalar ratio versus the scalar spectral index and tensor spectral index of the tachyon GB model with  $V = V_0 \phi^n$  and  $\mathcal{G} = \mathcal{G}_0 \phi^{-n}$ .

Table 5: The ranges of the parameter  $\beta$  in which the tensor-to-scalar ratio, the scalar spectral index and the tensor spectral index of the tachyon GB model with  $V = V_0 \phi^n$  and  $\mathcal{G} = \mathcal{G}_0 \phi^{-n}$  are consistent with different data sets.

Planck2018 TT,TE,EE+lowE +lensing+BK14+BAO		Planck2018 TT,TE,EE+lowE +lensing+BK14+BAO		Planck2018 TT,TE,EE+lowE lensing+BK14+BAO +LIGO&Virgo2016		Planck2018 TT,TE,EE+lowE lensing+BK14+BAO LIGO&Virgo2016	
$N$	68% CL		95% CL		68% CL		95% CL
$n = 2$	50	$0.360 \leq \beta < 1$		all values	$0.201 \leq \beta \leq 0.938$		all values
	60	not consistent		$0.251 \leq \beta < 1$	$0.042 \leq \beta \leq 0.924$		all values
	70	not consistent		not consistent	$\beta \leq 0.911$		all values
$n = 4$	50	$0.498 \leq \beta < 1$		$0.254 \leq \beta < 1$	$0.403 \leq \beta \leq 0.953$		$0.188 \leq \beta < 1$
	60	$0.685 \leq \beta < 0.892$		$0.205 \leq \beta < 1$	$0.283 \leq \beta \leq 0.943$		$0.020 \leq \beta < 1$
	70	not consistent		not consistent	$0.164 \leq \beta \leq 0.937$		all values

the tachyon model more observationally viable. Our numerical analysis shows that  $r - n_s$  in the tachyon GB inflation with  $V = V_0 \phi^n$  and  $\mathcal{G} = \mathcal{G}_0 \phi^{-n}$ , is consistent with 68% CL of the base data if  $N < 54.2$  for  $n = 2$  and  $N < 60.5$  for  $n = 4$ . In this case,  $r - n_s$  is consistent with 95% CL of base data if  $N < 62.4$  for  $n = 2$  and  $N < 70$  for  $n = 4$ .

The bottom panels of Figure 5 show the tensor-to-scalar ratio versus the tensor spectral index of the tachyon GB model with  $V = V_0 \phi^n$  and  $\mathcal{G} = \mathcal{G}_0 \phi^{-n}$ . The tachyon GB model is consistent with observational data in some ranges of  $\beta$ . In Table 5, we present the constraints on  $\beta$  for  $N = 50, 60, 70$  and  $n = 2, 4$  which makes the model observationally viable. In this regard, we find that the tachyon Gauss-Bonnet inflation with  $V = V_0 \phi^n$  and  $\mathcal{G} = \mathcal{G}_0 \phi^{-n}$  for  $n = 2$  and  $n = 4$  is consistent with observational data if  $\beta \sim \mathcal{O}(10^{-1})$ .

## 6.2 Power-Law Potential and Dilaton-Like GB Coupling

In this subsection, we consider the following potential and GB coupling

$$V = V_0 \phi^n \quad \& \quad \mathcal{G} = \mathcal{G}_0 e^{-\lambda \phi}. \quad (63)$$

Now, we have

$$n_s = 1 - \frac{-e^{\lambda \phi} \chi n^2 + \beta \lambda^2 \chi \phi^{n+2} - \beta \lambda \phi^{n+2} \chi' + e^{\lambda \phi} n \chi' \phi - e^{\lambda \phi} \chi n}{\phi (\phi^{n+1} \beta \lambda - n e^{\lambda \phi})}, \quad (64)$$

$$n_T = - \frac{(-\kappa^4 \beta \lambda e^{-\lambda \phi} + n \phi^{-n-1}) n}{\phi}, \quad (65)$$

and

$$r = 8 \frac{-e^{-2\lambda \phi} \phi^{n+1} \beta^2 \lambda^2 + 2 e^{-\lambda \phi} n \beta \lambda - \phi^{-n-1} n^2}{\phi}. \quad (66)$$

By using these perturbation parameters we perform a numerical analysis on the model. The top panels of Figure 6 show the behavior of  $r - n_s$  of the tachyon GB model with functions given

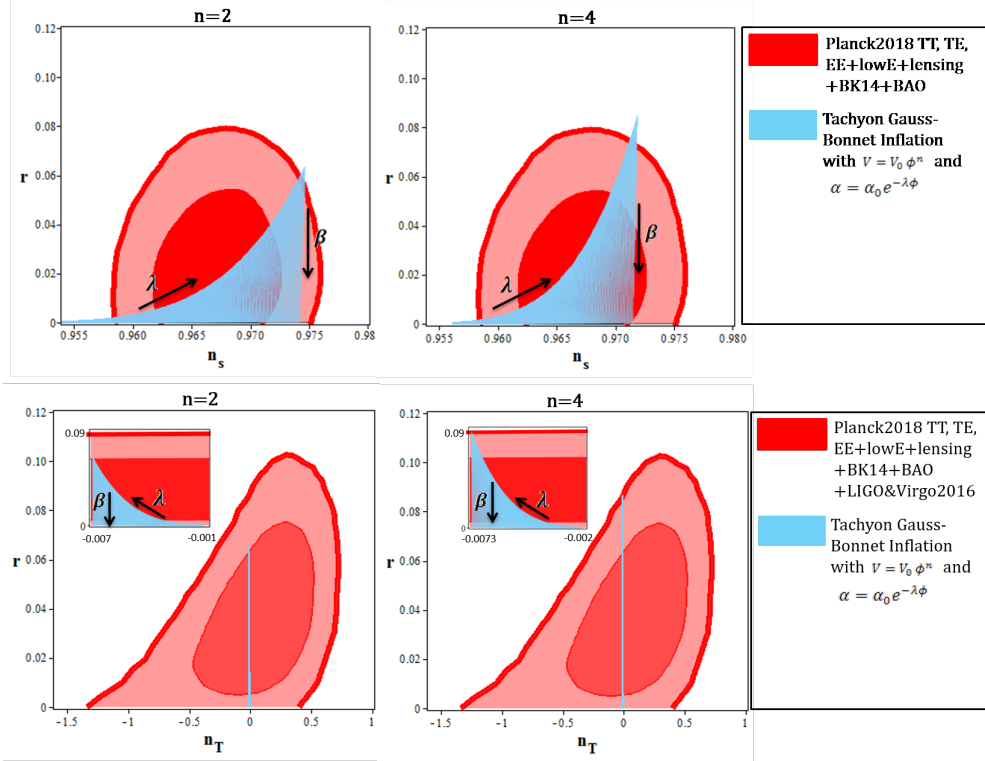


Figure 6: Tensor-to-scalar ratio versus the scalar spectral index and tensor spectral index of the tachyon GB model with  $V = V_0 \phi^n$  and  $\mathcal{G} = \mathcal{G}_0 e^{-\lambda \phi}$ .

by equation (63), in the background of the base data for  $N = 60$ . Our numerical analysis shows that, in this case, the tachyon GB model with  $0.15 < \lambda$  (for  $n = 2$ ) and  $0.10 < \lambda$  (for  $n = 4$ ) is consistent with the base data at 95% CL. Also, this model with  $0.19 < \lambda < 0.37$  (for  $n = 2$ ) and  $0.18 < \lambda < 0.52$  (for  $n = 4$ ) is consistent with the base data at 68% CL.

The tensor spectral index versus the tensor-to-scalar ratio of the tachyon GB model with  $V = V_0 \phi^n$  and  $\mathcal{G} = \mathcal{G}_0 e^{-\lambda \phi}$ , in the background of the base+GW data, is shown in the bottom panels of Figure 6. As figure shows, for all values of  $\lambda$  and  $\beta$ , the tensor-to-scalar ratio and the tensor spectral index of this model are consistent with base+GW data at 95% CL. However, there are some constraints on  $\lambda$  and  $\beta$  at 68% CL. At this level, the constraints on  $\lambda$  are  $0.23 < \lambda$  (for  $n = 2$ ) and  $0.19 < \lambda$  (for  $n = 4$ ). For some sample values of  $\lambda$ , the constraints on  $\beta$  are summarized in Table 6. According to this analysis, for the tachyon Gauss-Bonnet inflation with  $V = V_0 \phi^n$  and  $\mathcal{G} = \mathcal{G}_0 e^{-\lambda \phi}$  and for  $n = 2$ , we can't find any constraint on  $\beta$ . This is because, this model for all values of  $\beta$  is consistent with observational data at 95% CL. For  $n = 4$ , if we assume large values of  $\lambda$  as  $\lambda \sim \mathcal{O}(10^4)$ , we find that the constraint  $\beta \lesssim \mathcal{O}(10^{-2})$ .

Table 6: The ranges of the parameter  $\beta$  in which the tensor-to-scalar ratio, the scalar spectral index and the tensor spectral index of the tachyon GB model with  $V = V_0 \phi^n$  and  $\mathcal{G} = \mathcal{G}_0 e^{-\lambda\phi}$  are consistent with different data sets.

	Planck2018 TT,TE,EE+lowE +lensing+BK14+BAO	Planck2018 TT,TE,EE+lowE +lensing+BK14+BAO	Planck2018 TT,TE,EE+lowE lensing+BK14+BAO +LIGO&Virgo2016	Planck2018 TT,TE,EE+lowE lensing+BK14+BAO LIGO&Virgo2016
$N$	68% CL	95% CL	68% CL	95% CL
$n = 2$				
10	$\beta \leq 0.832$	all values of $\beta$	not consistent	all values of $\beta$
$10^2$	$0.421 \leq \beta \leq 0.683$	all values of $\beta$	$\beta \leq 0.742$	all values of $\beta$
$10^4$	not consistent	all values of $\beta$	$\beta \leq 0.839$	all values of $\beta$
$n = 4$				
10	all values of $\beta$	all values of $\beta$	not consistent	all values of $\beta$
$10^2$	$0.093 \leq \beta$	all values of $\beta$	$\beta \leq 0.886$	all values of $\beta$
$10^4$	$0.411 \leq \beta$	$0.046 \leq \beta$	$0.235 \leq \beta \leq 0.901$	all values of $\beta$

## 7 DBI Gauss-Bonnet Inflation

There is another proposal arisen from the string theory, which is based on the Dirac-Born-Infeld action [63, 64]. This proposal suggests that the field responsible for inflation is characterized by the radial coordinate of a D3 brane which moves in a “throat” (often  $AdS_5$  throat) region of a warped compactified space. Both the speed of the brane and the warp factor of the throat, set a speed limit upon the brane’s motion. In this model, besides the potential, there is a function of the scalar field related to the local geometry of the compact manifold traversed by the D3 brane. Also, the kinetic term of the field is non-canonical [63].

In the DBI model, we have

$$P(X, \phi) = -\mathcal{F}^{-1}(\phi) \sqrt{1 - 2\mathcal{F}(\phi)X} - V(\phi), \quad (67)$$

By this definition, the scalar spectral index takes the following forms

$$n_s = 1 - 2M\chi - \left[ 4M\chi^2 (\mathcal{F}^{-1} + V) \left( \frac{B}{M} + \frac{\chi'}{\chi} \right) - \frac{16}{3} \alpha' \chi^2 (\mathcal{F}^{-1} + V)^3 \right. \\ \left. \left( \frac{\alpha''}{\alpha'} + 2 \frac{-\frac{\mathcal{F}'}{\mathcal{F}^2} + V'}{\mathcal{F}^{-1} + V} + \frac{\chi'}{\chi} \right) \right] \left[ 2M\chi - \frac{8}{3} \alpha' \chi (\mathcal{F}^{-1} + V)^2 \right]^{-1}. \quad (68)$$

The tensor spectral index in DBI GB model is given by

$$n_T = -2M\chi, \quad (69)$$

and the tensor-to-scalar ratio is obtained as follows

$$r = -16M\chi + \frac{64}{3} \alpha' \chi (V + \mathcal{F}^{-1})^2, \quad (70)$$

where

$$\chi = \frac{1}{2} \frac{\frac{\mathcal{F}'}{\mathcal{F}^2} - V' - 24 H^4 \alpha'}{\kappa^2 (\mathcal{F}^{-1} + V)^2}, \quad (71)$$

$$M = \frac{\mathcal{F}'}{\mathcal{F}^2} - 4 \frac{\mathcal{F}' (\mathcal{F}^{-1} + V)^4 \chi^2}{\mathcal{F}} - V', \quad (72)$$

and

$$B = \frac{\mathcal{F}''}{\mathcal{F}^2} - 2 \frac{\mathcal{F}'^2}{\mathcal{F}^3} - 4 \frac{(\mathcal{F}'' \mathcal{F} - \mathcal{F}'^2) (\mathcal{F}^{-1} + V)^4 \chi^2}{\mathcal{F}^2} - 4 \frac{\mathcal{F}' \left( -4 \frac{\mathcal{F}'}{\mathcal{F}^2} + 4 V' \right) (\mathcal{F}^{-1} + V)^3 \chi^2}{\mathcal{F}} - 8 \frac{\mathcal{F}' (\mathcal{F}^{-1} + V)^4 \chi \chi'}{\mathcal{F}} - V''. \quad (73)$$

As pervious sections, by choosing some explicit functions for the potential and coupling function, we study this model numerically.

## 7.1 Power-Law potential and Inverse Power-Law GB Coupling

We start this subsection by adopting the following potential and GB coupling function

$$V = V_0 \phi^n, \quad \mathcal{F} = \mathcal{F}_0 \phi^{-n} \quad \& \quad \mathcal{G} = \mathcal{G}_0 \phi^{-n}. \quad (74)$$

In this case, we get

$$n_s = 1 - \frac{4 \mu \phi \beta \varphi^2 + 16 \phi^n n \beta \varphi - 8 \phi^n \varphi + 8 \phi^{n+1} \mu - 2 \phi^{-n} \varphi^5 + 2 \phi^{-n} n \beta \varphi^5 - 10 \phi^{-n} n \varphi^5}{4 \phi (2 \beta \phi^n + \varphi^2 - 2 \phi^n) (\varphi^2 - 2 \phi^n)} - \frac{-8 \phi^{n+1} \mu \beta + \phi^{-2n} n \varphi^7 + 6 \phi^{-n+1} \varphi^4 \mu + 24 \varphi^3 n - 12 n \beta \varphi^3 - 16 \phi^n n \varphi + 8 \phi^n \beta \varphi - 16 \varphi^2 \mu \phi}{4 \phi (2 \beta \phi^n + \varphi^2 - 2 \phi^n) (\varphi^2 - 2 \phi^n)} - \frac{-4 \beta \varphi^3 + 8 \varphi^3}{4 \phi (2 \beta \phi^n + \varphi^2 - 2 \phi^n) (\varphi^2 - 2 \phi^n)}, \quad (75)$$

$$n_T = - \frac{n^2 (16 \phi^{n-2} n^2 \beta^3 - 24 \phi^{n-2} n^2 \beta^2 + 12 \phi^{n-2} n^2 \beta - 2 \phi^{n-2} n^2 - 2 \beta + 1)}{\phi^2}, \quad (76)$$

and

$$r = 8 \frac{n^2 (2 \kappa^4 \beta - 1) (8 \phi^{n-2} n^2 \kappa^8 \beta^2 - 8 \phi^{n-2} n^2 \beta \kappa^4 + \kappa^4 \beta - \kappa^4 + 2 \phi^{n-2} n^2)}{\kappa^6 \phi^2}, \quad (77)$$

with

$$\varphi = 2 \phi^{n-1} n (2 \beta - 1), \quad (78)$$

and

$$\mu = 2 \phi^{n-2} n (2 \beta n - n - 2 \beta + 1). \quad (79)$$

Performing an analysis on the above scalar spectral index and tensor-to-scalar ratio gives Figure 7. Our numerical analysis shows that although the GB effect makes the DBI model observationally

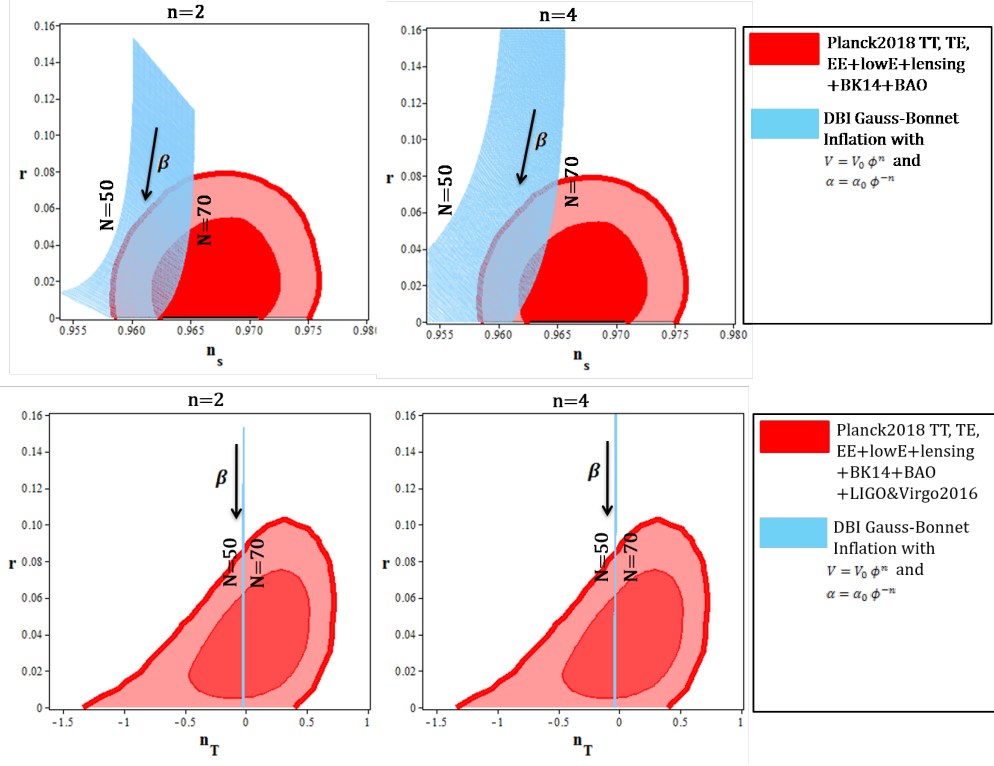


Figure 7: Tensor-to-scalar ratio versus the scalar spectral index and tensor spectral index of the DBI GB model with  $V = V_0 \phi^n$  and  $\mathcal{G} = \mathcal{G}_0 \phi^{-n}$ .

viable, but this viability happens with  $N > 52$  for  $n = 2$  and  $N > 59$  for  $n = 4$ . The bottom panels of Figure 7 show the tensor spectral index versus the tensor-to-scalar ratio of the DBI GB model with  $V = V_0 \phi^n$  and  $\mathcal{G} = \mathcal{G}_0 \phi^{-n}$ , in the background of the base+GW data. The ranges of the parameter  $\beta$  in which the scalar spectral index, the tensor spectral index and tensor to scalar ratio of this model are consistent with the base data at 68% CL and 95% CL, are summarized in Table 7. These considerations show that, the DBI Gauss-Bonnet inflation with  $V = V_0 \phi^n$  and  $\mathcal{G} = \mathcal{G}_0 \phi^{-n}$  for both  $n = 2$  and  $n = 4$  cases is consistent with observational data if  $\beta \lesssim \mathcal{O}(10^{-1})$  and  $N \gtrsim 60$ .

## 7.2 Power-Law Potential and Dilaton-Like GB Coupling

In this section, we consider the following potential and GB coupling

$$V = V_0 \phi^n, \quad \mathcal{F} = \mathcal{F}_0 \phi^{-n} \quad \& \quad \mathcal{G} = \mathcal{G}_0 e^{-\lambda \phi}, \quad (80)$$

which lead to

$$n_s = 1 - \frac{-\frac{nB}{\phi} + \frac{nA}{\phi \kappa^2}}{A^{-1} \kappa^2 B^2} - 2 \frac{n(-B\kappa^2 + A)(-2B^2 C \phi^n \kappa^2 + 6AB^2 C - A\phi^{n-1}n + A\phi^{n-1})}{B(-2nB\kappa^2 + 2nA + \beta \lambda e^{-\lambda \phi} \phi \kappa^2 B^2)(-\phi^n \kappa^2 + A)} - \frac{\beta \lambda e^{-\lambda \phi} (2C\kappa^2 B^2 \phi - \lambda \phi A + 2nA) B}{-2nB\kappa^2 + 2nA + \beta \lambda e^{-\lambda \phi} \phi \kappa^2 B^2}, \quad (81)$$



Table 7: The ranges of the parameter  $\beta$  in which the tensor-to-scalar ratio, the scalar spectral index and the tensor spectral index of the DBI GB model with  $V = V_0 \phi^n$  and  $\mathcal{G} = \mathcal{G}_0 \phi^{-n}$  are consistent with different data sets.

		Planck2018 TT,TE,EE+lowE +lensing+BK14+BAO	Planck2018 TT,TE,EE+lowE +lensing+BK14+BAO	Planck2018 TT,TE,EE+lowE lensing+BK14+BAO +LIGO&Virgo2016	Planck2018 TT,TE,EE+lowE lensing+BK14+BAO LIGO&Virgo2016
	$N$	68% CL	95% CL	68% CL	95% CL
$n = 2$	50	not consistent	not consistent	$0.617 \leq \beta < 1$	$0.411 \leq \beta < 1$
	60	not consistent	$0.613 \leq \beta \leq 0.948$	$0.607 \leq \beta < 1$	$0.352 \leq \beta < 1$
	70	$0.705 \leq \beta \leq 0.981$	$0.326 \leq \beta < 1$	$0.489 \leq \beta \leq 0.971$	$0.361 \leq \beta < 1$
$n = 4$	50	not consistent	not consistent	$0.733 \leq \beta < 1$	$0.674 \leq \beta < 1$
	60	not consistent	$0.683 \leq \beta \leq 0.915$	$0.712 \leq \beta \leq 0.980$	$0.676 \leq \beta < 1$
	70	$0.774 \leq \beta \leq 0.865$	$0.643 \leq \beta < 1$	$0.702 \leq \beta \leq 0.984$	$0.680 \leq \beta < 1$

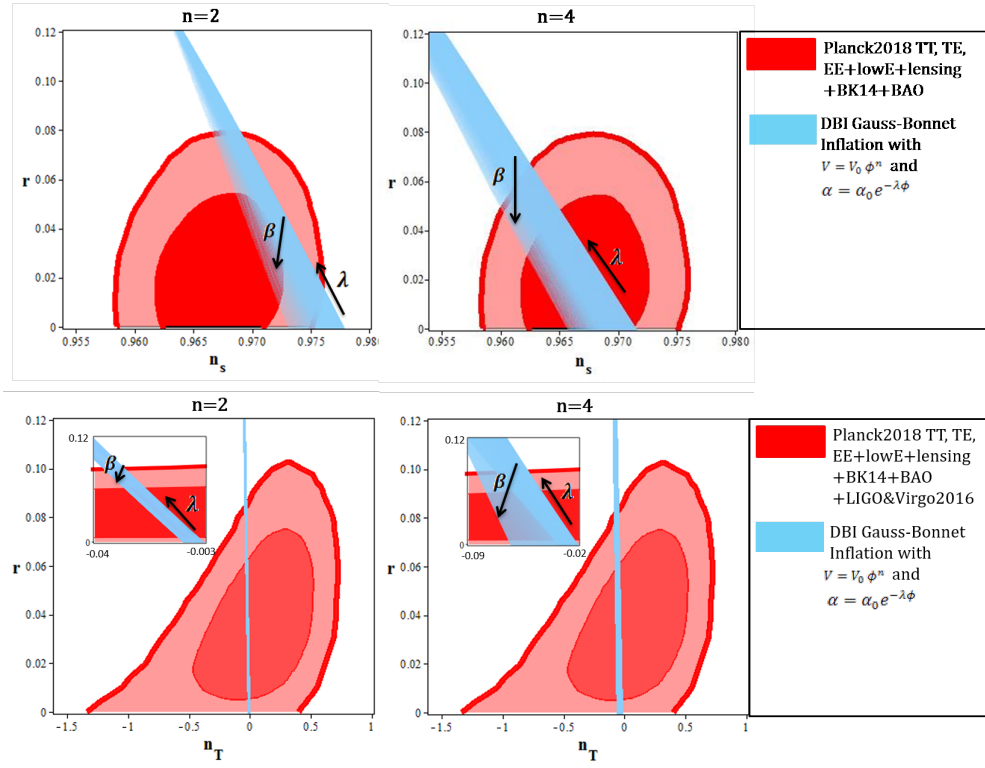


Figure 8: Tensor-to-scalar ratio versus the scalar spectral index and tensor spectral index of the DBI GB model with  $V = V_0 \phi^n$  and  $\mathcal{G} = \mathcal{G}_0 e^{-\lambda \phi}$ .

Table 8: The ranges of the parameter  $\beta$  in which the tensor-to-scalar ratio, the scalar spectral index and of the DBI GB model with  $V = V_0 \phi^n$  and  $\mathcal{G} = \mathcal{G}_0 e^{-\lambda\phi}$  are consistent with different data sets.

	Planck2018 TT,TE,EE+lowE +lensing+BK14+BAO	Planck2018 TT,TE,EE+lowE +lensing+BK14+BAO	Planck2018 TT,TE,EE+lowE lensing+BK14+BAO +LIGO&Virgo2016	Planck2018 TT,TE,EE+lowE lensing+BK14+BAO LIGO&Virgo2016
$N$	68% CL	95% CL	68% CL	95% CL
$n = 2$				
10	not consistent	$0.112 \leq \beta \leq 0.986$	$0.609 \leq \beta \leq 0.973$	$0.332 \leq \beta < 1$
$10^2$	$0.917 \leq \beta < 1$	all values	$0.607 \leq \beta \leq 0.970$	$0.329 \leq \beta < 1$
$10^4$	not consistent	$0.326 \leq \beta < 1$	$0.601 \leq \beta \leq 0.966$	$0.321 \leq \beta < 1$
$n = 4$				
10	all values	all values	$0.521 \leq \beta \leq 0.971$	$0.388 \leq \beta < 1$
$10^2$	$0.182 \leq \beta < 1$	all values	$0.518 \leq \beta \leq 0.969$	$0.381 \leq \beta < 1$
$10^4$	not consistent	$0.442 \leq \beta < 1$	$0.511 \leq \beta \leq 0.965$	$0.370 \leq \beta < 1$

with

$$B = \phi^n + \frac{1}{\phi^{-n}}, \quad (82)$$

$$A = -\frac{nB}{\phi} + \kappa^4 B^2 \beta \lambda e^{-\lambda\phi}, \quad (83)$$

and

$$C = \frac{1}{2} \left( -\frac{Bn^2}{\phi^2} + \frac{nB}{\phi^2} + 2 \frac{\kappa^4 B^2 \beta \lambda e^{-\lambda\phi} n}{\phi} - \kappa^4 B^2 \beta \lambda^2 e^{-\lambda\phi} \right) \kappa^{-2} B^{-2} - \frac{An}{B^2 \phi \kappa^2}. \quad (84)$$

The tensor spectral index is given by

$$n_T = -\frac{n(n\phi\kappa^2 - 2\phi^{n+2}\kappa^6\beta\lambda e^{-\lambda\phi} + n^2 - 4\phi^{n+1}n\kappa^4\beta\lambda e^{-\lambda\phi} + 4\phi^{2n+2}\kappa^8\beta^2\lambda^2 e^{-2\lambda\phi})}{\kappa^4\phi^3}. \quad (85)$$

The tensor-to-scalar ratio takes the following form

$$r = 8 \frac{n^2\phi\kappa^2 - 2\phi^{n+2}n\kappa^6\beta\lambda e^{-\lambda\phi} + n^3 - 4\phi^{n+1}n^2\kappa^4\beta\lambda e^{-\lambda\phi} + 4\phi^{2n+2}n\kappa^8\beta^2\lambda^2 e^{-2\lambda\phi}}{\kappa^4\phi^3} + 8 \frac{2\beta^2\lambda^2 e^{-2\lambda\phi}\kappa^6\phi^{3+2n} - \beta\lambda e^{-\lambda\phi}\kappa^2\phi^{n+2}n}{\kappa^4\phi^3}. \quad (86)$$

Now, we analyze these perturbation parameter numerically and the results are shown in Figure 8. Our numerical analysis shows that the GB effect makes the DBI model observationally viable. The ranges of the parameter  $\beta$  in which both the scalar spectral index and tensor to scalar ratio of this model are consistent with the base and base+GW data at 68% CL and 95% CL, are summarized in Table 8. These considerations show that, the DBI Gauss-Bonnet inflation with  $V = V_0 \phi^n$  and  $\mathcal{G} = \mathcal{G}_0 e^{-\lambda\phi}$  for both  $n = 2$  and  $n = 4$  cases is consistent with observational data if  $\beta \lesssim \mathcal{O}(10^{-1})$ .

## 8 Reheating Phase in a Gauss-Bonnet Model with Canonical Scalar Field

The reheating process after inflation is necessary to reheat the universe for subsequent evolution. Actually, this process can explain the cosmic origin of the matter component of the universe [83, 112]. The production of cosmic relics, such as photons and neutrinos, can be explained by considering the process of reheating in the universe [113, 114]. Also, the reheating phase accounts for the observed matter-antimatter asymmetry in the universe [115, 116]. By studying the reheating process in the Gauss-Bonnet models, we can find more constraints on the model's parameter space. To study this process, we focus on two important parameters  $N_{rh}$  and  $T_{rh}$  (where subscript  $rh$  stands for reheating). We obtain some expressions for these parameters in terms of the scalar spectral index, which let us to compare the model with observational data (see Refs. [93, 94, 95, 96, 97]). By using the following expression

$$N_{hc} = \ln \left( \frac{a_e}{a_{hc}} \right), \quad (87)$$

we define the e-folds number between the time when the physical scales cross the horizon and the time when the inflation ends. The subscripts  $hc$  and  $e$  show the value of the parameter at the horizon crossing and end of inflation, respectively. For the energy density during the reheating epoch, we have the relation  $\rho \sim a^{-3(1+\omega_{eff})}$ , with  $\omega_{eff}$  being the effective equation of state corresponding to the dominant energy density in the universe. Therefore, the e-folds number is written in terms of  $\rho$  and  $\omega_{eff}$  as follows

$$N_{rh} = \ln \left( \frac{a_{rh}}{a_e} \right) = -\frac{1}{3(1+\omega_{eff})} \ln \left( \frac{\rho_{rh}}{\rho_e} \right), \quad (88)$$

At the horizon crossing ( $k = aH$ ) we have

$$0 = \ln \left( \frac{k_{hc}}{a_{hc} H_{hc}} \right) = \ln \left( \frac{a_e}{a_{hc}} \frac{a_{rh}}{a_e} \frac{a_0}{a_{rh}} \frac{k_{hc}}{a_0 H_{hc}} \right), \quad (89)$$

where the subscript 0 shows the value of the scale factor at the current time. From equations (42), (43) and (44) we obtain

$$N_{hc} + N_{rh} + \ln \left( \frac{k_{hc}}{a_0 H_{hc}} \right) + \ln \left( \frac{a_0}{a_{rh}} \right) = 0. \quad (90)$$

To rewrite  $\frac{a_0}{a_{rh}}$  in terms of temperature and density, we use the following expression [95, 97]

$$\rho_{rh} = \frac{\pi^2 g_{rh}}{30} T_{rh}^4, \quad (91)$$

where the parameter  $g_{rh}$  is the effective number of the relativistic species at the reheating era. Also, the conservation of the entropy gives [95, 97]

$$\frac{a_0}{a_{rh}} = \left( \frac{43}{11g_{rh}} \right)^{-\frac{1}{3}} \frac{T_{rh}}{T_0}, \quad (92)$$

where the subscript 0 denotes the current value of the temperature. Now, from equations (91) and (92), we find the following expression for the scale factor

$$\frac{a_0}{a_{rh}} = \left( \frac{43}{11g_{rh}} \right)^{-\frac{1}{3}} T_0^{-1} \left( \frac{\pi^2 g_{rh}}{30\rho_{rh}} \right)^{-\frac{1}{4}}. \quad (93)$$

In the GB model with a canonical scalar field, we can write the energy density as follows

$$\rho = \left( 1 + \frac{\epsilon}{3} \right) V - \frac{160}{27} \kappa^6 \alpha'^2 V^3 - \frac{20}{9} \kappa^2 \alpha' V' V. \quad (94)$$

To obtain the energy density at the end of inflation era, we set  $\epsilon = 1$ . Then, we find

$$\rho_e = \frac{4}{3} V_e - \frac{160}{27} \kappa^6 \alpha_e'^2 V_e^3 - \frac{20}{9} \kappa^2 \alpha_e' V_e' V_e. \quad (95)$$

Now, by using equations (88) and (95) we obtain

$$\rho_{rh} = \left[ \frac{4}{3} V_e - \frac{160}{27} \kappa^6 \alpha_e'^2 V_e^3 - \frac{20}{9} \kappa^2 \alpha_e' V_e' V_e \right] \times \exp \left[ -3N_{rh}(1 + \omega_{eff}) \right]. \quad (96)$$

By using equations (93) and (96), we find the following expression for the scale factor

$$\begin{aligned} \ln \left( \frac{a_0}{a_{rh}} \right) = & -\frac{1}{3} \ln \left( \frac{43}{11g_{rh}} \right) - \frac{1}{4} \ln \left( \frac{\pi^2 g_{rh}}{30\rho_{rh}} \right) - \ln T_0 - \frac{3}{4} N_{rh}(1 + \omega_{eff}) \\ & + \frac{1}{4} \ln \left( \frac{4}{3} V_e - \frac{160}{27} \kappa^6 \alpha_e'^2 V_e^3 - \frac{20}{9} \kappa^2 \alpha_e' V_e' V_e \right). \end{aligned} \quad (97)$$

To obtain  $N_{rh}$ , we find  $H_{hc}$  from equation (14). After that, by using equations (90) and (97), we obtain the e-folds number during reheating as follows

$$\begin{aligned} N_{rh} = \frac{4}{1 - 3\omega_{eff}} \left[ -N_{hc} - \ln \left( \frac{k_{hc}}{a_0 T_0} \right) - \frac{1}{4} \ln \left( \frac{40}{\pi^2 g_{rh}} \right) + \frac{1}{2} \ln \left( 8\pi^2 \mathcal{A}_s \mathcal{W}_s c_s^3 \right) - \frac{1}{3} \ln \left( \frac{11g_{rh}}{43} \right) \right. \\ \left. - \frac{1}{4} \ln \left( \frac{4}{3} V_e - \frac{160}{27} \kappa^6 \alpha_e'^2 V_e^3 - \frac{20}{9} \kappa^2 \alpha_e' V_e' V_e \right) \right]. \end{aligned} \quad (98)$$

The temperature during reheating is obtained from equations (88), (92) and (95) as follows

$$T_{rh} = \left( \frac{30}{\pi^2 g_{rh}} \right)^{\frac{1}{4}} \left[ \frac{4}{3} V_e - \frac{160}{27} \kappa^6 \alpha_e'^2 V_e^3 - \frac{20}{9} \kappa^2 \alpha_e' V_e' V_e \right]^{\frac{1}{4}} \times \exp \left[ -\frac{3}{4} N_{rh}(1 + \omega_{eff}) \right]. \quad (99)$$

To perform a numerical analysis, it is useful to write equations (98) and (99) in terms of the scalar spectral index. To this end, we should specify the potential and GB coupling. In the following, we adopt the potential and GB coupling used in the previous sections and explore each case separately.

Table 9: Constraints on the e-folds number and temperature during the reheating phase in the GB model with canonical scalar field and with  $V = V_0 \phi^n$  and  $\mathcal{G} = \mathcal{G}_0 \phi^{-n}$ , obtained from Planck2018 TT, TE, EE+lowE+lensing+BK14+BAO joint data.

		$\omega = -1$	$\omega = -\frac{1}{3}$	$\omega = 0$	$\omega = 1$
$n = 2$	$0.680 \leq \beta < 1$	$N_{rh} < 7.4$	$N_{rh} < 12.37$	$N_{rh} < 23.35$	all values of $N_{rh}$
$n = 2$	$0.680 \leq \beta < 1$	$\log_{10} \left( \frac{T_{rh}}{GeV} \right) > 14.16$	$\log_{10} \left( \frac{T_{rh}}{GeV} \right) > 7.96$	$\log_{10} \left( \frac{T_{rh}}{GeV} \right) > -0.73$	all values of $T_{rh}$

### 8.1 Power-Law potential and Inverse Power-Law GB Coupling

In this case, we use the potential and GB coupling defined in equation (29). As we have seen before, in this case the GB model only with  $n = 2$  is consistent with the base data. Therefore, we use equation (29) with  $n = 2$ , find the final values of the potential and GB coupling in terms of the scalar field at the horizon crossing and substitute them in equations (98) and (99). After that, we obtain the scalar field at horizon crossing in terms of the scalar spectral index. By considering the value of the scalar spectral index, obtained from the base data, we find some constraints on the e-folds number and temperature during the reheating phase. In studying the  $r - n_s$  behavior with equation (19), the tightest constraint on  $\beta$  has been obtained as  $0.680 \leq \beta < 1$ . To numerically analyze of the reheating phase, we use this constraint and four values of  $\omega$  as  $\omega = -1, -\frac{1}{3}, 0$  and  $1$ . The results are presented in Table 9. The behavior of  $N_{rh}$  and  $T_{rh}$  versus  $n_s$ , for  $\beta = 0.7$ , has been shown in Figure 9. Note that, as the top left panel of Figure 9 shows, all curves converge to  $N_{rh} = 0$  (corresponding to instantaneous reheating process) and  $n_s = 0.965$  which is observationally viable from base data.

The bottom panel of Figure 9 shows the range of  $N_{rh}$  and  $\omega_{eff}$ , in the case considered in this subsection, leading to the observationally viable values of the scalar spectral index. As figure shows, when  $\omega_{eff}$  changes from  $-1$  (field's potential domination) to  $\frac{1}{3}$  (radiation domination) the values of  $N_{rh}$  increase. This means that, the reheating phase of the universe is not instantaneous and lasts some e-folds.

The parameter  $N_{rh}$ , which describes the duration of the reheating phase, is related to the scalar spectral index of the perturbations. To have viable reheating phase,  $N_{rh}$  should be consistent with observational value of  $n_s$ . Any small variation of  $N_{rh}$  can lead to the values of  $n_s$  which are not observationally viable. Therefore, the reheating phase should last until some specific values and not more than it. In this regard, we have tried to obtain some precise values of the parameters leading to the viable GB models.

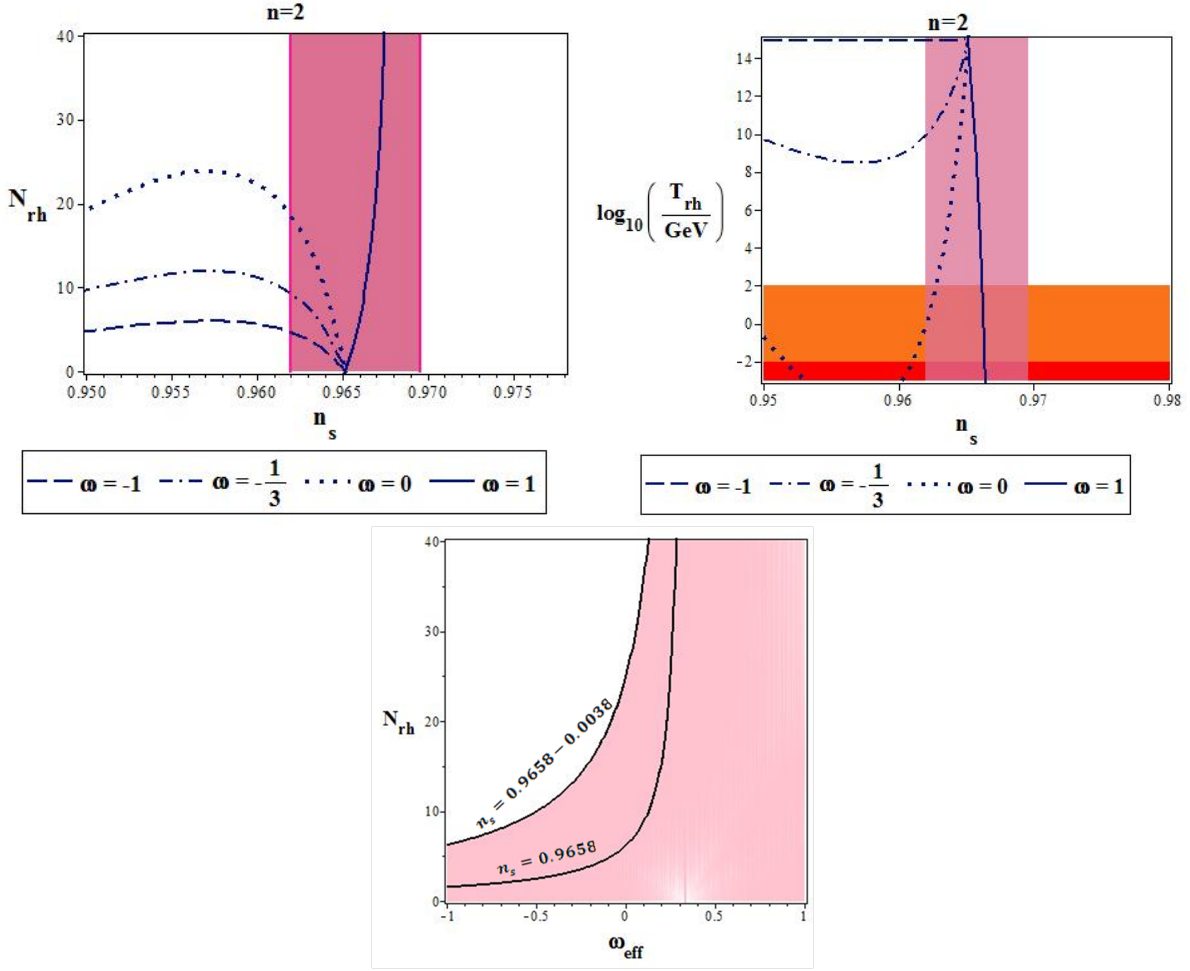


Figure 9: Behavior of the e-folds number (top left panel) and temperature (top right panel) during the reheating phase versus  $n_s$ , and the range of  $N_{rh}$  and  $\omega_{eff}$  leading to the observationally viable values of the scalar spectral index (bottom panel), in the GB model with canonical scalar field and with  $V = V_0 \phi^2$  and  $\mathcal{G} = \mathcal{G}_0 \phi^{-2}$ . The magenta region in the top panels shows the values of the scalar spectral index released by Planck2018 TT, TE, EE+lowE+lensing+BK14+BAO joint data. In the top right panel, the orange region corresponds to the temperatures below the electroweak scale,  $T < 100$  GeV and the red region corresponds to the temperatures below the big bang nucleosynthesis scale,  $T < 10$  MeV.

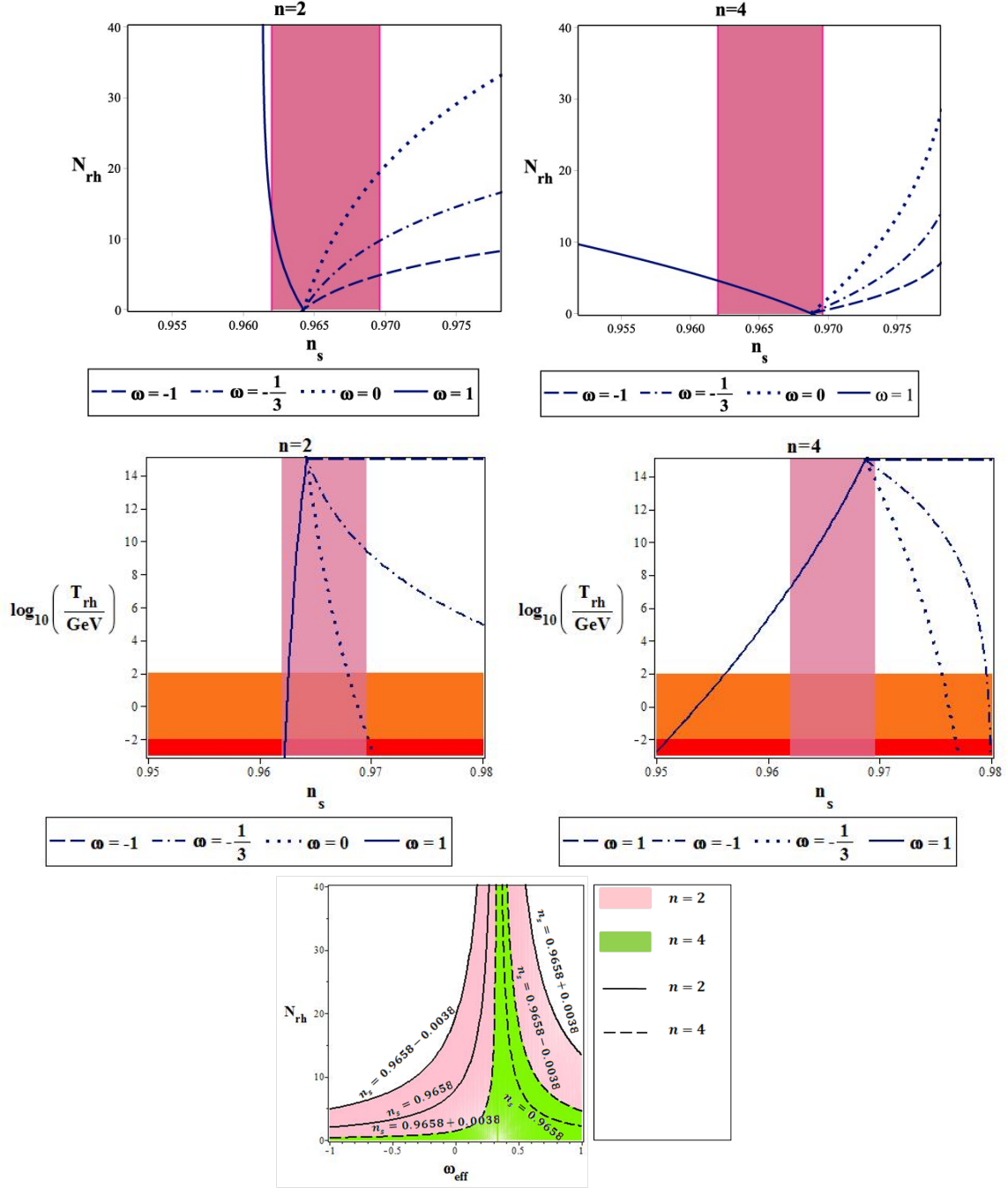


Figure 10: Behavior of the e-folds number (top left panel) and temperature (top right panel) during the reheating phase versus the scalar spectral index, and the range of  $N_{rh}$  and  $\omega_{eff}$  leading to the observationally viable values of the scalar spectral index (bottom panel), in the GB model with canonical scalar field and with  $V = V_0 \phi^2$  and  $\mathcal{G} = \mathcal{G}_0 \phi^{-2}$ . The magenta region in the top panels shows the values of the scalar spectral index released by Planck2018 TT, TE, EE+lowE+lensing+BK14+BAO joint data. In the top right panel, the orange region corresponds to the temperatures below the electroweak scale,  $T < 100$  GeV and the red region corresponds to the temperatures below the big bang nucleosynthesis scale,  $T < 10$  MeV.

Table 10: Constraints on the e-folds number and temperature during the reheating phase in the GB model with canonical scalar field and with  $V = V_0 \phi^n$  and  $\mathcal{G} = \mathcal{G}_0 e^{-\lambda\phi}$ , obtained from Planck2018 TT, TE, EE+lowE+lensing+BK14+BAO joint data.

		$\omega = -1$	$\omega = -\frac{1}{3}$	$\omega = 0$	$\omega = 1$
$n = 2$	$0.031 \leq \beta < 0.072$	$N_{rh} < 6.85$	$N_{rh} < 11.47$	$N_{rh} < 22.66$	$N_{rh} < 16.72$
$n = 4$	$0.670 \leq \beta \leq 0.716$	$N_{rh} < 0.56$	$N_{rh} < 1.42$	$N_{rh} < 2.37$	$N_{rh} < 5.14$
$n = 2$	$0.031 \leq \beta < 0.072$	$\log_{10} \left( \frac{T_{rh}}{\mathcal{G}eV} \right) > 14.09$	$\log_{10} \left( \frac{T_{rh}}{\mathcal{G}eV} \right) > 8.65$	$\log_{10} \left( \frac{T_{rh}}{\mathcal{G}eV} \right) > -2.21$	all values of $T_{rh}$
$n = 4$	$0.670 \leq \beta \leq 0.716$	$\log_{10} \left( \frac{T_{rh}}{\mathcal{G}eV} \right) > 14.18$	$\log_{10} \left( \frac{T_{rh}}{\mathcal{G}eV} \right) > 14.53$	$\log_{10} \left( \frac{T_{rh}}{\mathcal{G}eV} \right) > 13.22$	$\log_{10} \left( \frac{T_{rh}}{\mathcal{G}eV} \right) > 6.27$

## 8.2 Power-Law Potential and Dilaton-Like GB Coupling

In this subsection, we use the potential and GB coupling defined in equation (34). We have shown that, in this case the GB model with both  $n = 2$  and  $n = 4$ , in some ranges of the parameters is consistent with the observational data. By using the adopted potential and GB coupling, we study the e-folds number and temperature in the reheating phase numerically and find some constraints on these parameters in confrontation with the base data. To obtain the constraints, we use the ranges of  $\beta$  from Table 2. In  $n = 2$  case, the tightest constraint on  $\beta$  is  $0.031 \leq \beta \leq 0.072$  and in  $n = 4$  case we have  $0.670 \leq \beta \leq 0.716$ . With these ranges of  $\beta$ , we obtain the constraints shown in Table 10. The behavior of  $N_{rh}$  and  $T_{rh}$  versus  $n_s$ , for  $\beta = 0.7$ , has been shown in the top and middle panels of Figure 10.

The bottom panel of Figure 10 shows the range of  $N_{rh}$  and  $\omega_{eff}$ , in the case considered in this subsection, leading to the observationally viable values of the scalar spectral index. In this case also, when  $\omega_{eff}$  changes from  $-1$  to  $\frac{1}{3}$ , the values of  $N_{rh}$  increase. This means that, the reheating phase of the universe is not instantaneous and lasts some e-folds. However, this figure shows another point too. For  $\omega_{eff} > \frac{1}{3}$ , by increasing the values of the effective equation of state parameter the values of  $N_{rh}$  decrease. Therefore, in this case, the value of  $\omega_{eff}$  does not become larger than  $\frac{1}{3}$ , because the e-folds number just increases and can not decrease.

## 8.3 Gauss-Bonnet Natural Inflation

Now, we study the reheating phase in the GB natural inflation model. By using (38), we study the e-folds number and temperature in the reheating phase numerically and find some constraints on these parameters. In this case, the tightest constraint obtained from the base data at 95% CL is  $0.525 \leq \beta < 1$  (see Table 3). The numerical results corresponding to this constraint, are shown in Table 11. The behavior of  $N_{rh}$  and  $T_{rh}$  versus  $n_s$ , for  $\beta = 0.7$ , has been shown in the top panels of Figure 11. As figure shows, the instantaneous reheating in this case is corresponding to  $n_s = 0.965$  which is observationally viable.

The bottom panel of Figure 11 shows the range of  $N_{rh}$  and  $\omega_{eff}$ , in the GB natural inflation model, leading to the observationally viable values of the scalar spectral index. As figure shows,



Table 11: Constraints on the e-folds number and temperature during the reheating phase in the GB natural inflation, obtained from Planck2018 TT, TE, EE+lowE+lensing+BK14+BAO joint data.

	$\omega = -1$	$\omega = -\frac{1}{3}$	$\omega = 0$	$\omega = 1$
$0.525 \leq \beta < 1$	$N_{rh} < 2.85$	$N_{rh} < 4.84$	$N_{rh} < 10.42$	$N_{rh} < 5.11$
$0.525 \leq \beta < 1$	$\log_{10} \left( \frac{T_{rh}}{GeV} \right) > 14.04$	$\log_{10} \left( \frac{T_{rh}}{GeV} \right) > 12.95$	$\log_{10} \left( \frac{T_{rh}}{GeV} \right) > 10.45$	$\log_{10} \left( \frac{T_{rh}}{GeV} \right) > 9.71$

the reheating phase of the universe described by GB natural inflation is not instantaneous. In this case also, the value of  $\omega_{eff}$  does not become larger than  $\frac{1}{3}$ .

## 8.4 Gauss-Bonnet $\alpha$ -attractor

To study the reheating phase in the GB  $\alpha$ -attractor model, we consider both E-model and T-Model types of potential and GB coupling. In the following we present the results for each case.

### 8.4.1 E-Model

In this case we adopt the E-Model potential and GB coupling defined in equation (42). As before, by using these functions, we study the e-folds number and temperature in reheating phase numerically. With E-Model potential and GB coupling, the tightest constraint obtained from the base data at 95% CL is  $\beta \leq 4.81 \times 10^{-2}$ . This range of  $\beta$  leads to the constraints presented in Table 12. To obtain these constraints, we have set  $\alpha = 50$ . The behavior of  $N_{rh}$  and  $T_{rh}$  versus  $n_s$ , for  $\beta = 0.03$ , has been shown in the top and middle panels of Figure 12. In this case, the instantaneous reheating, corresponding to  $n_s = 0.965$ , is observationally viable. The bottom panel of Figure 12 shows the range of  $N_{rh}$  and  $\omega_{eff}$  leading to the observationally viable values of the scalar spectral index.

### 8.4.2 T-Model

Now, we consider the T-Model potential and GB coupling defined in equation (47). In this case also, we analyze the e-folds number and temperature in the reheating phase in confrontation with observational data. With T-Model potential and GB coupling, the tightest constraint on  $\beta$ , obtained from the base data at 95% CL, is  $\beta \leq 7.01 \times 10^{-2}$  (see Table 4). The numerical results of the T-model case with  $\beta \leq 7.01 \times 10^{-2}$  and  $\alpha = 50$  are shown in Table 12. The behavior of  $N_{rh}$  and  $T_{rh}$  versus  $n_s$ , for  $\beta = 0.03$ , has been shown in Figure 12. Here also, the instantaneous reheating is favored by observational data. The bottom panel of Figure 12 shows the range of  $N_{rh}$  and  $\omega_{eff}$ , in the case considered in this subsection, leading to the observationally viable values of the scalar spectral index. According to our numerical analysis, in the GB  $\alpha$ -attractor model with both E-model and T-model functions, the reheating phase of the universe is not instantaneous and the value of  $\omega_{eff}$  does not become larger than  $\frac{1}{3}$ .

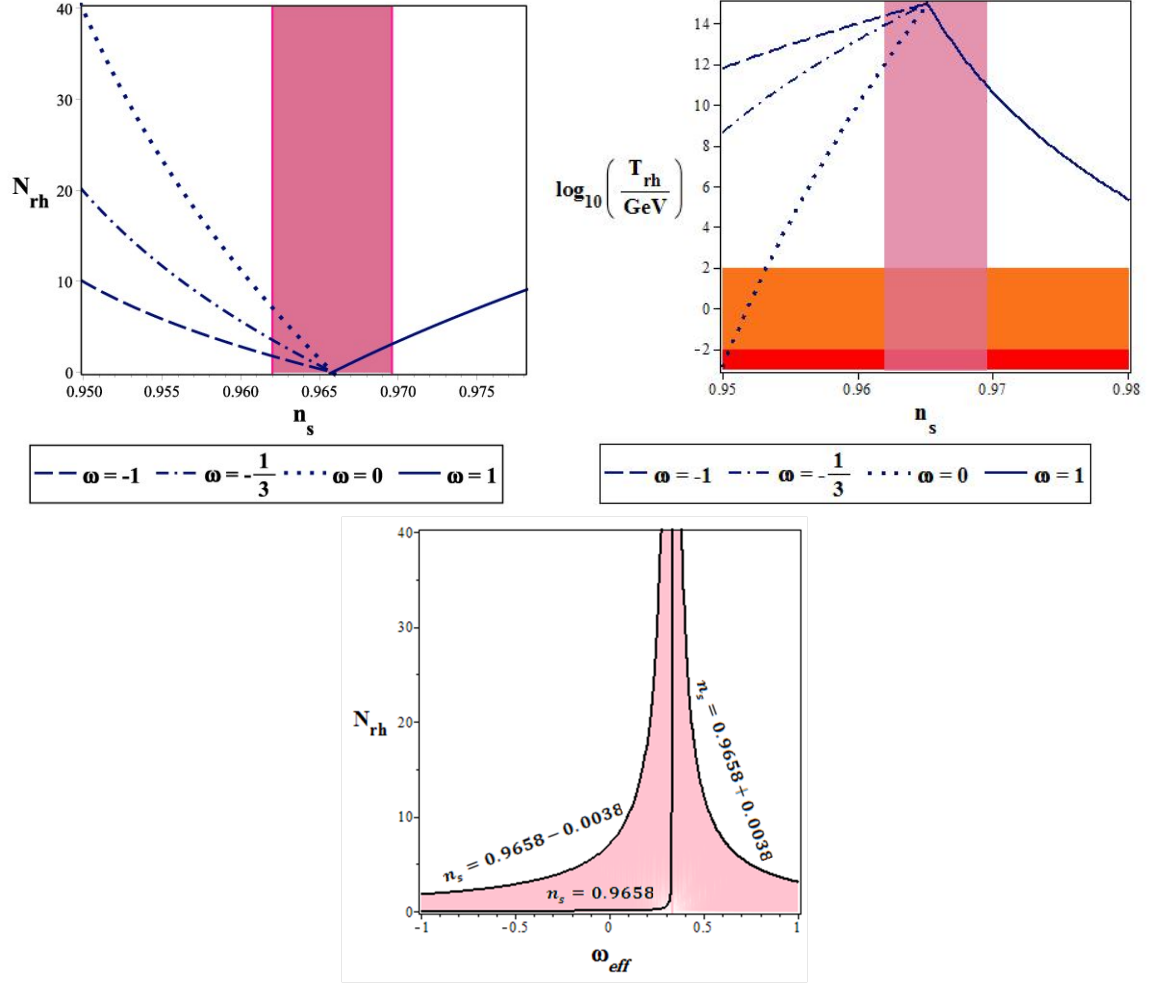


Figure 11: Behavior of the e-folds number (top left panel) and temperature (top right panel) during the reheating phase versus the scalar spectral index, and the range of  $N_{rh}$  and  $\omega_{eff}$  leading to the observationally viable values of the scalar spectral index (bottom panel), in the GB natural inflation.

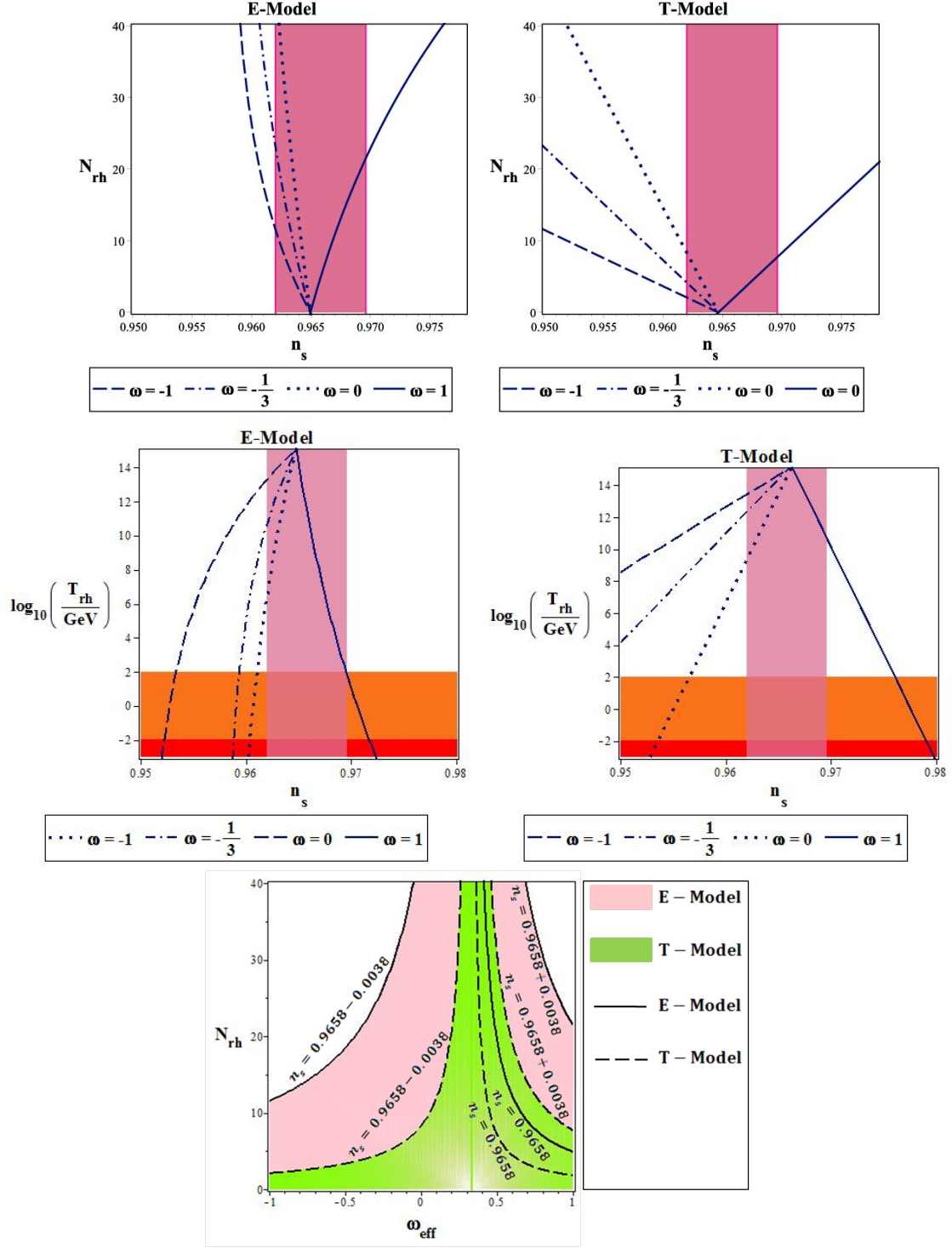


Figure 12: Behavior of the e-folds number (top panels) and temperature (middle panels) the reheating phase versus the scalar spectral index, and the range of  $N_{rh}$  and  $\omega_{eff}$  leading to the observationally viable values of the scalar spectral index (bottom panel), in the GB  $\alpha$ -attractor model.

Table 12: Constraints on the e-folds number and temperature during the reheating phase in the GB  $\alpha$ -attractor model, obtained from Planck2018 TT, TE, EE+lowE+lensing+BK14+BAO joint data.

		$\omega = -1$	$\omega = -\frac{1}{3}$	$\omega = 0$	$\omega = 1$
E-Model	$\beta \leq 4.81 \times 10^{-2}$	$N_{rh} \leq 16.825$	$N_{rh} \leq 37.521$	$N_{rh} \leq 52.647$	$N_{rh} \leq 26.367$
T-Model	$\beta \leq 7.01 \times 10^{-2}$	$N_{rh} \leq 4.110$	$N_{rh} \leq 7.334$	$N_{rh} \leq 12.45$	$N_{rh} \leq 10.14$
E-Model	$\beta \leq 4.81 \times 10^{-2}$	$\log_{10} \left( \frac{T_{rh}}{GeV} \right) \geq 12.49$	$\log_{10} \left( \frac{T_{rh}}{GeV} \right) \geq 8.73$	$\log_{10} \left( \frac{T_{rh}}{GeV} \right) \geq 4.73$	$\log_{10} \left( \frac{T_{rh}}{GeV} \right) \geq 0.266$
T-Model	$\beta \leq 7.01 \times 10^{-2}$	$\log_{10} \left( \frac{T_{rh}}{GeV} \right) \geq 12.66$	$\log_{10} \left( \frac{T_{rh}}{GeV} \right) \geq 10.21$	$\log_{10} \left( \frac{T_{rh}}{GeV} \right) \geq 7.12$	$\log_{10} \left( \frac{T_{rh}}{GeV} \right) \geq 8.37$

## 9 Reheating in a Gauss-Bonnet Model with Tachyon Field

In this section, we study the reheating process in a Gauss-Bonnet model with tachyon field. Here, we can use the equations (88)-(93) of section 8. However, the energy density and the equation of motion in the tachyon GB model are different from the GB model with canonical scalar field. In this regard, we have

$$\rho = V \left( 1 - \frac{2}{3}\epsilon - \frac{64}{27}\kappa^6 V^2 \alpha'^2 - \frac{8}{3}\kappa^2 \alpha' V' \right)^{-\frac{1}{2}} - \frac{64}{9}\kappa^6 V^2 \alpha'^2 - \frac{8}{3}\kappa^2 \alpha' V'. \quad (100)$$

At the end of inflation ( $\epsilon = 1$ ) we obtain

$$\rho_e = V_e \left( \frac{1}{3} - \frac{64}{27}\kappa^6 V_e^2 \alpha_e'^2 - \frac{8}{3}\kappa^2 \alpha_e' V_e' \right)^{-\frac{1}{2}} - \frac{64}{9}\kappa^6 V_e^2 \alpha_e'^2 - \frac{8}{3}\kappa^2 \alpha_e' V_e'. \quad (101)$$

Now, by using equations (88) and (101) we reach

$$\rho_{rh} = \left[ V_e \left( \frac{1}{3} - \frac{64}{27}\kappa^6 V_e^2 \alpha_e'^2 - \frac{8}{3}\kappa^2 \alpha_e' V_e' \right)^{-\frac{1}{2}} - \frac{64}{9}\kappa^6 V_e^2 \alpha_e'^2 - \frac{8}{3}\kappa^2 \alpha_e' V_e' \right] \times \exp \left[ -3N_{rh}(1 + \omega_{eff}) \right]. \quad (102)$$

Equations (93) and (102) give the following expression for the scale factor

$$\ln \left( \frac{a_0}{a_{rh}} \right) = -\frac{1}{3} \ln \left( \frac{43}{11g_{rh}} \right) - \frac{1}{4} \ln \left( \frac{\pi^2 g_{rh}}{30\rho_{rh}} \right) - \ln T_0 - \frac{3}{4} N_{rh}(1 + \omega_{eff}) + \frac{1}{4} \ln \left[ V_e \left( \frac{1}{3} - \frac{64}{27}\kappa^6 V_e^2 \alpha_e'^2 - \frac{8}{3}\kappa^2 \alpha_e' V_e' \right)^{-\frac{1}{2}} - \frac{64}{9}\kappa^6 V_e^2 \alpha_e'^2 - \frac{8}{3}\kappa^2 \alpha_e' V_e' \right]. \quad (103)$$

Table 13: Constraints on the e-folds number and temperature during the reheating phase in the tachyon GB model with  $V = V_0 \phi^n$  and  $\mathcal{G} = \mathcal{G}_0 \phi^{-n}$ , obtained from Planck2018 TT, TE, EE+lowE+lensing+BK14+BAO joint data.

		$\omega = -1$	$\omega = -\frac{1}{3}$	$\omega = 0$	$\omega = 1$
$n = 2$	$0.251 \leq \beta < 1$	$N_{rh} \leq 5.65$	$N_{rh} \leq 9.86$	$N_{rh} \leq 19.62$	not consistent
$n = 4$	$0.254 \leq \beta < 1$	$N_{rh} \leq 4.73$	$N_{rh} \leq 7.88$	$N_{rh} \leq 15.87$	not consistent
$n = 2$	$0.251 \leq \beta < 1$	$\log_{10} \left( \frac{T_{rh}}{GeV} \right) \geq 12.59$	$\log_{10} \left( \frac{T_{rh}}{GeV} \right) \geq 8.62$	$\log_{10} \left( \frac{T_{rh}}{GeV} \right) \geq 2.54$	not consistent
$n = 4$	$0.254 \leq \beta < 1$	$\log_{10} \left( \frac{T_{rh}}{GeV} \right) \geq 12.03$	$\log_{10} \left( \frac{T_{rh}}{GeV} \right) \geq 9.42$	$\log_{10} \left( \frac{T_{rh}}{GeV} \right) \geq 15.87$	not consistent

To find  $N_{rh}$ , as before, we use  $H_{hc}$  obtained from equation (14). Then, using (90) and (103) gives the e-folds number during the reheating process as follows

$$N_{rh} = \frac{4}{1 - 3\omega_{eff}} \left\{ -N_{hc} - \ln \left( \frac{k_{hc}}{a_0 T_0} \right) - \frac{1}{4} \ln \left( \frac{40}{\pi^2 g_{rh}} \right) + \frac{1}{2} \ln \left( 8\pi^2 \mathcal{A}_s \mathcal{W}_s c_s^3 \right) - \frac{1}{3} \ln \left( \frac{11g_{rh}}{43} \right) \right. \\ \left. - \frac{1}{4} \ln \left[ V_e \left( \frac{1}{3} - \frac{64}{27} \kappa^6 V_e^2 \alpha_e'^2 - \frac{8}{3} \kappa^2 \alpha_e' V_e' \right)^{-\frac{1}{2}} - \frac{64}{9} \kappa^6 V_e^2 \alpha_e'^2 - \frac{8}{3} \kappa^2 \alpha_e' V_e' \right] \right\}. \quad (104)$$

From equations (88), (92) and (101), we get the following expression for the temperature during the reheating process

$$T_{rh} = \left( \frac{30}{\pi g_{rh}} \right)^{\frac{1}{4}} \left[ V_e \left( \frac{1}{3} - \frac{64}{27} \kappa^6 V_e^2 \alpha_e'^2 - \frac{8}{3} \kappa^2 \alpha_e' V_e' \right)^{-\frac{1}{2}} - \frac{64}{9} \kappa^6 V_e^2 \alpha_e'^2 - \frac{8}{3} \kappa^2 \alpha_e' V_e' \right] \\ \times \exp \left[ -\frac{3}{4} N_{rh} (1 + \omega_{eff}) \right]. \quad (105)$$

In the following, and to perform a numerical analysis, we adopt the potential and GB function used in section 6 and explore each case separately.

### 9.1 Power-Law potential and Inverse Power-Law GB Coupling

The first case we consider here is the tachyon GB model with power-law potential and inverse power-law GB coupling (equation (59)). We find the final values of these adopted functions in

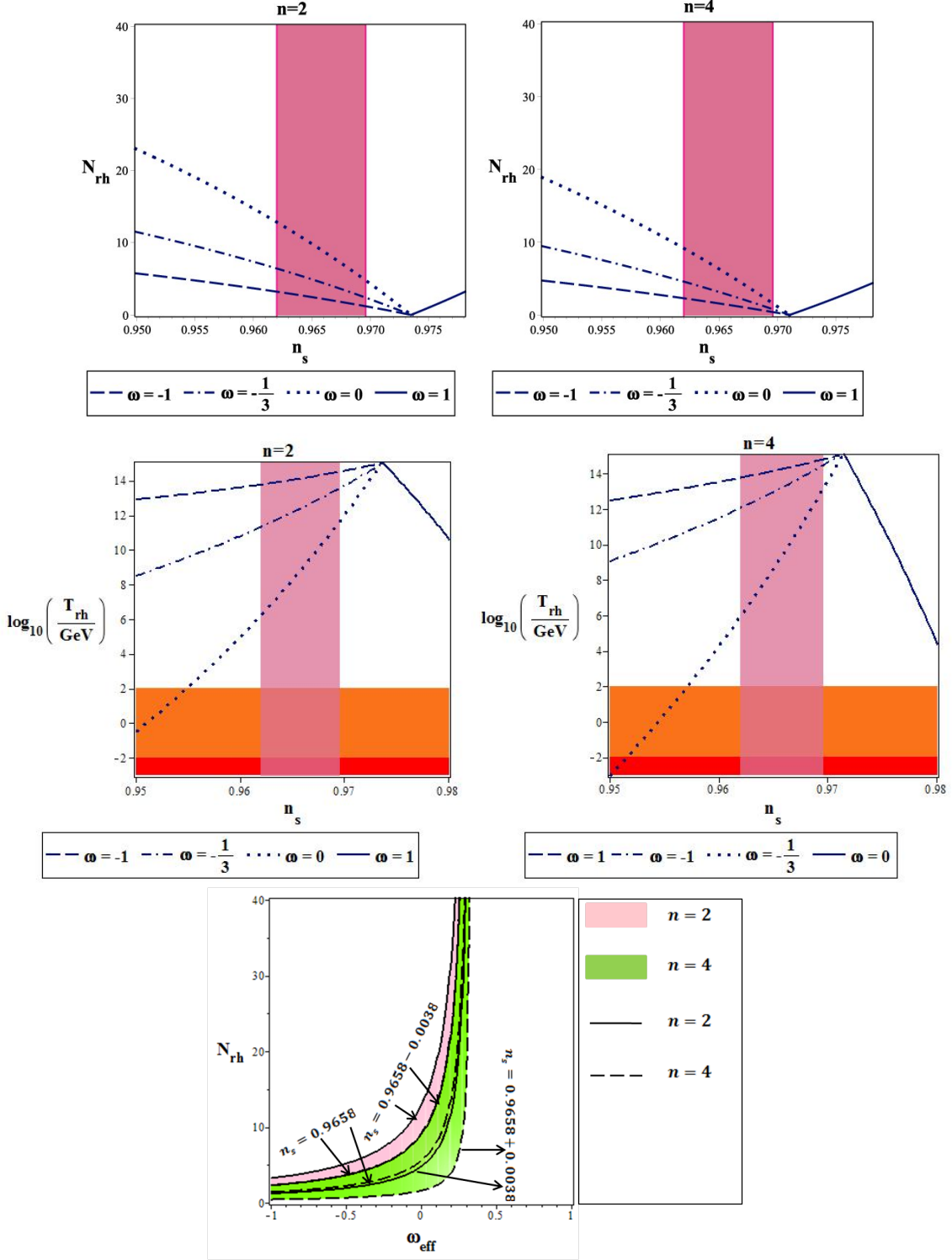


Figure 13: Behavior of the e-folds number (top panels) and temperature (middle panels) during the reheating phase versus the scalar spectral index, and the range of  $N_{rh}$  and  $\omega_{eff}$  leading to the observationally viable values of the scalar spectral index (bottom panel), in the tachyon GB model with  $V = V_0 \phi^n$  and  $\mathcal{G} = \mathcal{G}_0 \phi^{-n}$ .

Table 14: Constraints on the e-folds number and temperature during the reheating phase in the tachyon GB model with  $V = V_0 \phi^n$  and  $\mathcal{G} = \mathcal{G}_0 e^{-\lambda\phi}$ , obtained from Planck2018 TT, TE, EE+lowE+lensing+BK14+BAO joint data.

	$\beta$	$\omega = -1$	$\omega = -\frac{1}{3}$	$\omega = 0$	$\omega = 1$
$n = 2$	$0.023 \leq \beta < 1$	$N_{rh} \leq 5.73$	$N_{rh} \leq 12.39$	$N_{rh} \leq 20.04$	$N_{rh} \leq 16.42$
$n = 4$	$0.046 \leq \beta < 1$	$N_{rh} \leq 4.23$	$N_{rh} \leq 8.11$	$N_{rh} \leq 14.81$	$N_{rh} \leq 17.76$
$n = 2$	$0.023 \leq \beta < 1$	$\log_{10} \left( \frac{T_{rh}}{GeV} \right) \geq 11.480$	$\log_{10} \left( \frac{T_{rh}}{GeV} \right) \geq 7.41$	$\log_{10} \left( \frac{T_{rh}}{GeV} \right) \geq 3.11$	$\log_{10} \left( \frac{T_{rh}}{GeV} \right) \geq 6.53$
$n = 4$	$0.046 \leq \beta < 1$	$\log_{10} \left( \frac{T_{rh}}{GeV} \right) \geq 13.07$	$\log_{10} \left( \frac{T_{rh}}{GeV} \right) \geq 11.90$	$\log_{10} \left( \frac{T_{rh}}{GeV} \right) \geq 8.91$	$\log_{10} \left( \frac{T_{rh}}{GeV} \right) \geq 8.03$

terms of the scalar field at the horizon crossing and substitute them in equations (104) and (105). Then, by obtaining the scalar field at horizon crossing in terms of the scalar spectral index, we rewrite  $N_{rh}$  and  $T_{rh}$  in terms of  $n_s$  and perform a numerical analysis. As demonstrated in Table 5, we have the tightest ranges on  $\beta$  for  $n = 2$  as  $0.251 \leq \beta < 1$  and for  $n = 4$  as  $0.254 \leq \beta < 1$ . These ranges of  $\beta$  give the results summarized in Table 13.

The behavior of  $N_{rh}$  and  $T_{rh}$  versus  $n_s$ , for  $\beta = 0.7$ , has been shown in the top and middle panels of Figure 13. As figure shows, the instantaneous reheating in this case is corresponding to  $n_s = 0.971$  for  $n = 2$  and  $n_s = 0.974$  for  $n = 4$ . Therefore, in this case the instantaneous reheating is not observationally viable. The bottom panel of Figure 13 shows the range of  $N_{rh}$  and  $\omega_{eff}$ , in the case considered in this subsection, leading to the observationally viable values of the scalar spectral index.

## 9.2 Power-Law Potential and Dilaton-Like GB Coupling

Now, by using equation (63), we rewrite the e-folds number and temperature during reheating in terms of the scalar spectral index and perform a numerical analysis on the model. As we see from Figure 6, this model in most ranges of the parameter's space is consistent with observational data. In this case, for the considered sample values of  $\lambda$ , all values of  $\beta$  are observationally viable. However if we adopt very large values of  $\lambda$ , there would be some constraints on  $\beta$ . For instance, we take  $\lambda \sim 10^5$  and find  $0.0023 \leq \beta < 1$  for  $n = 2$  and  $0.046 \leq \beta < 1$  for  $n = 4$ . To analyze the reheating phase numerically, we use this ranges of  $\beta$  which lead to the constraints presented in Table 14.

The behavior of  $N_{rh}$  and  $T_{rh}$  versus  $n_s$ , for  $\beta = 0.7$ , has been shown in Figure 14. As figure shows, in this case the instantaneous reheating is observationally viable. The bottom panel of Figure 14 shows the range of  $N_{rh}$  and  $\omega_{eff}$ , in the case considered in this subsection, leading to the observationally viable values of the scalar spectral index.

In summary, our study shows that in the tachyon GB model with  $V = V_0 \phi^n$  and  $\mathcal{G} = \mathcal{G}_0 \phi^{-n}$ , there is no chance to have  $N_{rh} = 0$  in a observationally viable range. Therefore, considering that the reheating phase should start with  $N_{rh} = 0$ , this model is ruled out. Also, the tachyon GB

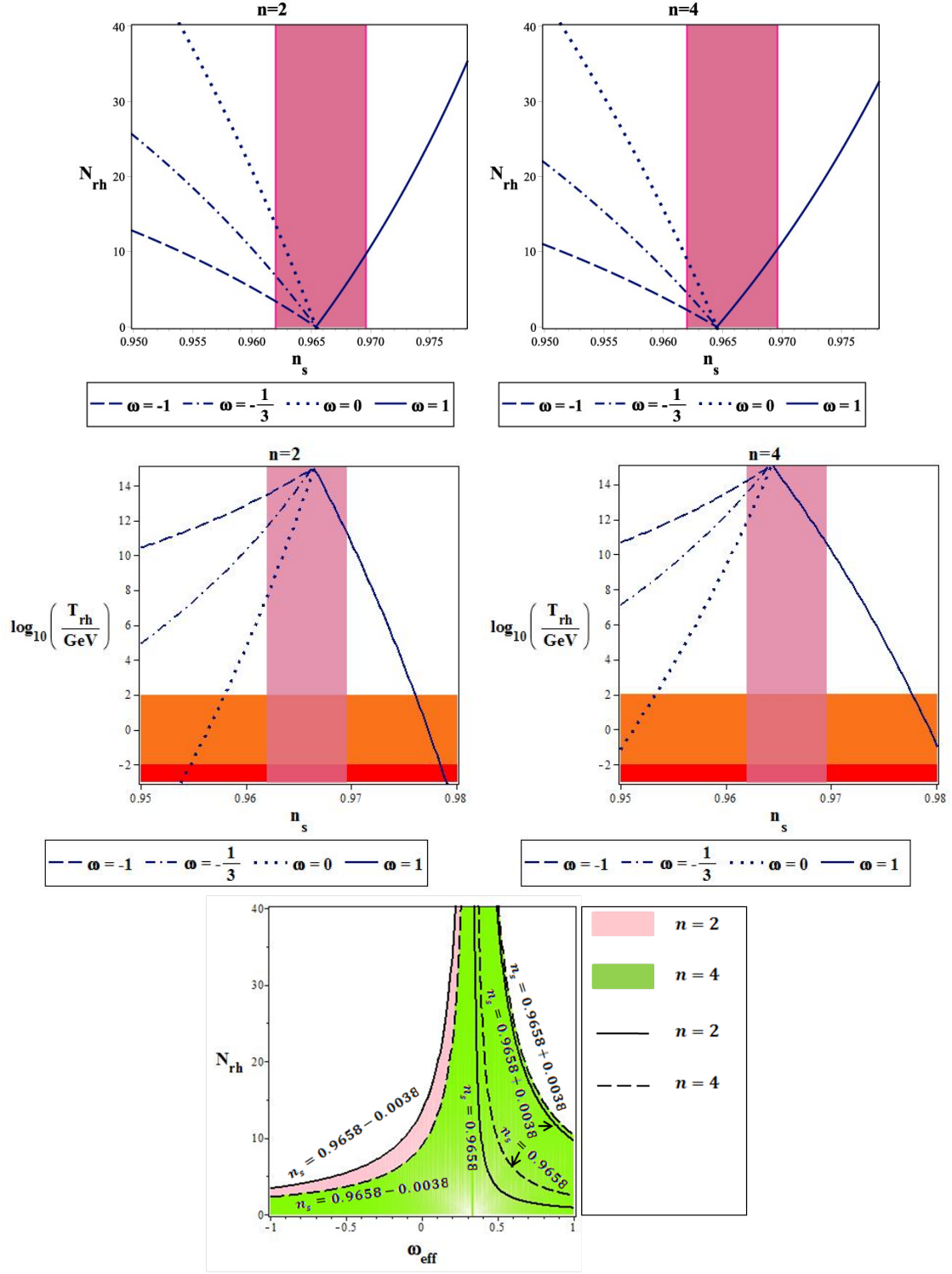


Figure 14: Behavior of the e-folds number (top panels) and temperature (middle panels) during the reheating phase versus the scalar spectral index, and the range of  $N_{rh}$  and  $\omega_{eff}$  leading to the observationally viable values of the scalar spectral index (bottom panel), in the tachyon GB model with  $V = V_0 \phi^n$  and  $V = V_0 \phi^n$  and  $\mathcal{G} = \mathcal{G}_0 e^{-\lambda\phi}$ .



model with  $V = V_0 \phi^n$  and  $\mathcal{G} = \mathcal{G}_0 e^{-\lambda\phi}$ , predicts that by increasing the value of  $N_{rh}$ , the value of  $\omega_{eff}$  increases until it reaches  $\frac{1}{3}$ . As before, the larger values of  $\omega_{eff}$  are not of interest.

## 10 Reheating in the DBI-Gauss-Bonnet Model

In this section, we study the reheating process in the DBI Gauss-Bonnet model. Here also, we can use the equations (88)-(93) of section 8, whereas, the energy density and the equation of motion in the DBI GB model are different from those in the GB model with canonical and also tachyon scalar fields. In the DBI GB model we have

$$\rho = f^{-1} \left( 1 + \frac{2}{3} \epsilon (1 + fV) - \frac{64}{27} f \alpha'^2 \kappa^4 (f^{-1} + V)^3 \right)^{-\frac{1}{2}} + V + \frac{8}{3} \alpha' (f^{-1} + V) \left( f' f^{-2} - V' - \frac{8}{3} \kappa^4 \alpha' (f^{-1} + V)^2 \right). \quad (106)$$

We obtain the following expression at the end of inflation ( $\epsilon = 1$ )

$$\rho_e = f_e^{-1} \left( 1 + \frac{2}{3} (1 + f_e V_e) - \frac{64}{27} f_e \alpha_e'^2 \kappa^4 (f_e^{-1} + V_e)^3 \right)^{-\frac{1}{2}} + V_e + \frac{8}{3} \alpha_e' (f_e^{-1} + V_e) \left( f_e' f_e^{-2} - V_e' - \frac{8}{3} \kappa^4 \alpha_e' (f_e^{-1} + V_e)^2 \right). \quad (107)$$

Now, by using equations (88) and (107), we find the following expression for the energy density during the reheating phase

$$\rho_{rh} = \left[ f_e^{-1} \left( 1 + \frac{2}{3} (1 + f_e V_e) - \frac{64}{27} f_e \alpha_e'^2 \kappa^4 (f_e^{-1} + V_e)^3 \right)^{-\frac{1}{2}} + V_e + \frac{8}{3} \alpha_e' (f_e^{-1} + V_e) \left( f_e' f_e^{-2} - V_e' - \frac{8}{3} \kappa^4 \alpha_e' (f_e^{-1} + V_e)^2 \right) \right] \times \exp \left[ -3N_{rh}(1 + \omega_{eff}) \right]. \quad (108)$$

From equations (93) and (108) we reach

$$\begin{aligned} \ln \left( \frac{a_0}{a_{rh}} \right) &= -\frac{1}{3} \ln \left( \frac{43}{11g_{rh}} \right) - \frac{1}{4} \ln \left( \frac{\pi^2 g_{rh}}{30\rho_{rh}} \right) - \ln T_0 - \frac{3}{4} N_{rh}(1 + \omega_{eff}) \\ &+ \frac{1}{4} \ln \left[ f_e^{-1} \left( 1 + \frac{2}{3} (1 + f_e V_e) - \frac{64}{27} f_e \alpha_e'^2 \kappa^4 (f_e^{-1} + V_e)^3 \right)^{-\frac{1}{2}} + V_e + \frac{8}{3} \alpha_e' (f_e^{-1} + V_e) \left( f_e' f_e^{-2} - V_e' - \frac{8}{3} \kappa^4 \alpha_e' (f_e^{-1} + V_e)^2 \right) \right]. \end{aligned} \quad (109)$$

Then, by using (90) and (109), we obtain the e-folds number during reheating as follows

$$N_{rh} = \frac{4}{1 - 3\omega_{eff}} \left\{ -N_{hc} - \ln\left(\frac{k_{hc}}{a_0 T_0}\right) - \frac{1}{4} \ln\left(\frac{40}{\pi^2 g_{rh}}\right) + \frac{1}{2} \ln\left(8\pi^2 \mathcal{A}_s \mathcal{W}_s c_s^3\right) - \frac{1}{3} \ln\left(\frac{11g_{rh}}{43}\right) \right. \\ \left. - \frac{1}{4} \ln \left[ f_e^{-1} \left( 1 + \frac{2}{3} (1 + f_e V_e) - \frac{64}{27} f_e \alpha_e'^2 \kappa^4 (f_e^{-1} + V_e)^3 \right)^{-\frac{1}{2}} + V_e + \frac{8}{3} \alpha_e' (f_e^{-1} + V_e) \right. \right. \\ \left. \left. \left( f_e' f_e^{-2} - V_e' - \frac{8}{3} \kappa^4 \alpha_e' (f_e^{-1} + V_e)^2 \right) \right] \right\}. \quad (110)$$

From equations (88), (92) and (106), we get the temperature during reheating as follows

$$T_{rh} = \left( \frac{30}{\pi g_{rh}} \right)^{\frac{1}{4}} \left[ V_e \left( \frac{1}{3} - \frac{64}{27} \kappa^6 V_e^2 \alpha_e'^2 - \frac{8}{3} \kappa^2 \alpha_e' V_e' \right)^{-\frac{1}{2}} - \frac{64}{9} \kappa^6 V_e^2 \alpha_e'^2 - \frac{8}{3} \kappa^2 \alpha_e' V_e' \right] \\ \times \exp \left[ -\frac{3}{4} N_{rh} (1 + \omega_{eff}) \right]. \quad (111)$$

In the following, we study the reheating phase in the DBI GB model numerically.

### 10.1 Power-Law potential and Inverse Power-Law GB Coupling

Here, we adopt power-law potential and inverse power-law GB coupling (equation (74) and obtain the final values of these adopted functions in terms of the scalar field at the horizon crossing and substitute in equations (110) and (111). By obtaining the scalar field at the horizon crossing in terms of the scalar spectral index, we rewrite  $N_{rh}$  and  $T_{rh}$  in terms of  $n_s$  and perform a numerical analysis. As Table 7 shows, we have the tightest range on  $\beta$  as  $0.613 \leq \beta \leq 0.948$  for  $n = 2$  and  $0.683 \leq \beta \leq 0.915$  for  $n = 4$ . In Table 15, we show the observational constraints on  $N_{rh}$  and  $T_{rh}$ , obtained from the mentioned ranges of  $\beta$ .

In the top and middle panels of Figure 15 we see the behavior of  $N_{rh}$  and  $T_{rh}$  versus  $n_s$ , for  $\beta = 0.7$ . The instantaneous reheating in this case, is not observationally viable. The bottom panel of Figure 15 shows the range of  $N_{rh}$  and  $\omega_{eff}$ , in the case considered in this subsection, leading to the observationally viable values of the scalar spectral index.

### 10.2 Power-Law Potential and Dilaton-Like GB Coupling

Now, we consider the DBI Gauss-Bonnet model with power-law potential and Dilaton-Like GB coupling (equation (80)). This model in some ranges of the parameter's space is consistent with observational data (see Table 8). In fact, for  $n = 2$ , we have the tightest range on  $\beta$  as  $0.326 \leq \beta \leq 0.986$  and for  $n = 4$  we have  $0.404 \leq \beta < 1$ . By these ranges of  $\beta$  we perform numerical analysis which gives the constraints shown in Table 16.

The behavior of  $N_{rh}$  and  $T_{rh}$  versus  $n_s$ , for  $\beta = 0.6$ , has been shown in Figure 16. As figure shows, with  $n = 2$  the instantaneous reheating is not observationally viable and with  $n = 4$  it is viable. The bottom panel of Figure 16 shows the range of  $N_{rh}$  and  $\omega_{eff}$ , in the case considered in this subsection, leading to the observationally viable values of the scalar spectral index.

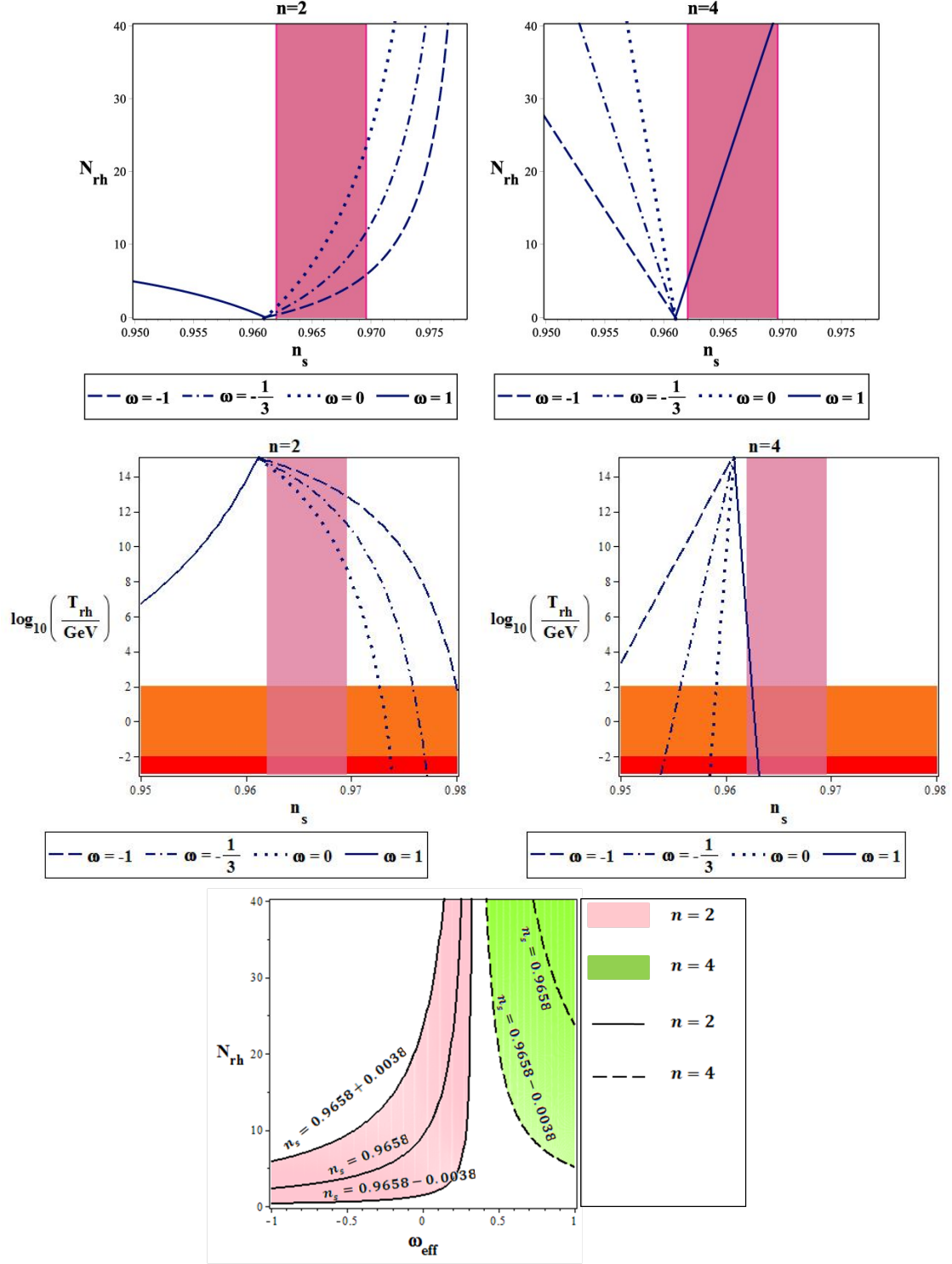


Figure 15: Behavior of the e-folds number (top panels) and temperature (middle panels) during the reheating phase versus the scalar spectral index, and the range of  $N_{rh}$  and  $\omega_{eff}$  leading to the observationally viable values of the scalar spectral index (bottom panel), in the DBI GB model with  $V = V_0 \phi^n$  and  $\mathcal{G} = \mathcal{G}_0 \phi^{-n}$ .

Table 15: Constraints on the e-folds number and temperature during the reheating phase in the DBI GB model with  $V = V_0 \phi^n$  and  $\mathcal{G} = \mathcal{G}_0 \phi^{-n}$ , obtained from Planck2018 TT, TE, EE+lowE+lensing+BK14+BAO joint data.

	$\omega = -1$		$\omega = -\frac{1}{3}$		$\omega = 0$	$\omega = 1$
$n = 2$	$0.613 \leq \beta \leq 0.948$	$0.141 < N_{rh} < 9.08$	$0.411 < N_{rh} < 19.43$	$0.561 < N_{rh} < 30.04$	not consistent	
$n = 4$	$0.683 \leq \beta \leq 0.915$	not consistent	not consistent	not consistent	$1.86 < N < 52.14$	
$n = 2$	$0.613 \leq \beta \leq 0.948$	$11.86 < \log_{10} \left( \frac{T_{rh}}{GeV} \right) < 14.97$	$9.12 < \log_{10} \left( \frac{T_{rh}}{GeV} \right) < 14.91$	$6.11 < \log_{10} \left( \frac{T_{rh}}{GeV} \right) < 14.86$	not consistent	
$n = 4$	$0.683 \leq \beta \leq 0.915$	not consistent	not consistent	not consistent	$\log_{10} \left( \frac{T_{rh}}{GeV} \right) < 7.42$	

According to these numerical considerations, in the DBI GB model with  $V = V_0 \phi^n$  and  $\mathcal{G} = \mathcal{G}_0 \phi^{-n}$ , for  $n = 2$ , there is no chance to have observationally viable  $N_{rh} = 0$ . Therefore, this case is ruled out. For  $n = 4$ , the model doesn't predict  $\omega_{eff} \leq \frac{1}{3}$  in the observationally viable regions. So, this case is ruled out too. In the DBI GB model with  $V = V_0 \phi^n$  and  $\mathcal{G} = \mathcal{G}_0 e^{-\lambda\phi}$ , the case with  $n = 2$  is not observationally viable. However, the case with  $n = 4$  is consistent with observational data. In fact, this case also predicts that by increasing the value of  $N_{rh}$ , the value of  $\omega_{eff}$  increases until it reaches  $\frac{1}{3}$ .

## 11 Summary

In this paper, we have studied inflation and reheating in several Gauss-Bonnet models. At first, we have considered a general GB model and presented the main equations of the the model in the inflation era. In this regard, we have obtained some important perturbation parameters such as the scalar spectral index, tensor spectral index and tensor-to-scalar ratio. Then, we have considered several GB models and studied the perturbation parameters numerically. By comparing the results with observational data, we have obtained some constraints on the model's parameter space. We have also analyzed the reheating epoch in each model and explored the model's viability in this context too. Our studies give the following results:

- Although the simple single filed inflation with  $\phi^2$  potential is not consistent with base and base+GW data sets, considering the GB effect with  $\phi^{-2}$  coupling, makes the model with  $\phi^2$  potential observationally viable. In this case, when the GB effect becomes larger, the tensor-to-scalar ratio becomes smaller and lies in the base data region at 95% CL. We have studied the cases with  $N = 50$ ,  $N = 60$  and  $N = 70$  for both  $r - n_s$  and  $r - n_T$  trajectories. The constraint obtained from these studied cases is as  $0.680 \leq \beta < 1$ . However, even by including the GB effect, the model with  $\phi^4$  potential is not observationally viable. We have also analyzed the reheating phase in the simple single filed inflation with  $\phi^2$  potential. Our

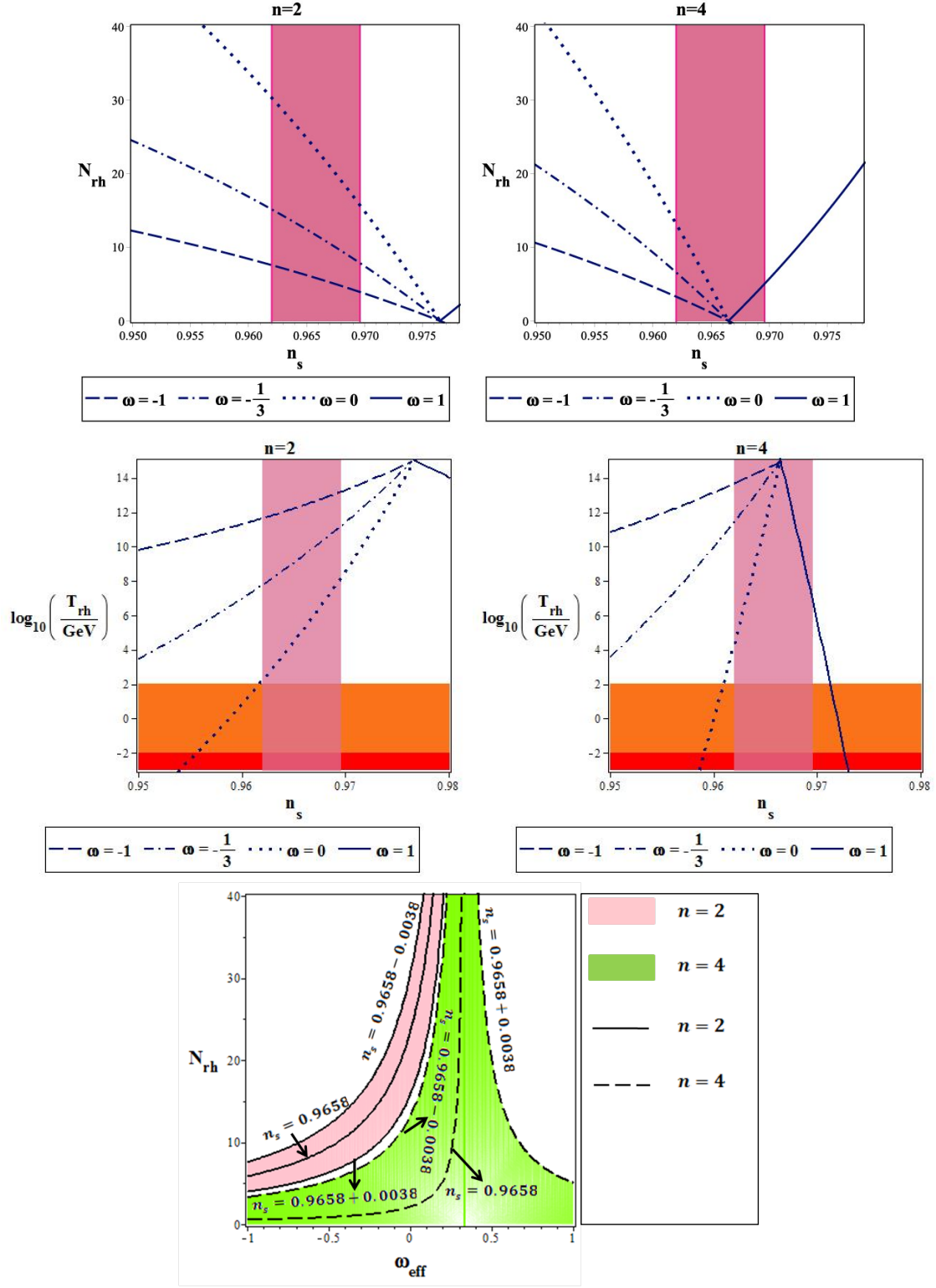


Figure 16: Behavior of the e-folds number (top panels) and temperature (middle panels) during the reheating phase versus the scalar spectral index, and the range of  $N_{rh}$  and  $\omega_{eff}$  leading to the observationally viable values of the scalar spectral index (bottom panel), in the DBI GB model with  $V = V_0 \phi^n$  and  $\mathcal{G} = \mathcal{G}_0 e^{-\lambda\phi}$ .

Table 16: Constraints on the e-folds number and temperature during the reheating phase in the DBI GB model with  $V = V_0 \phi^n$  and  $\mathcal{G} = \mathcal{G}_0 e^{-\lambda\phi}$ , obtained from Planck2018 TT, TE, EE+lowE+lensing+BK14+BAO joint data.

	$\omega = -1$	$\omega = -\frac{1}{3}$	$\omega = 0$	$\omega = 1$	
$n = 2$	$0.326 \leq \beta \leq 0.986$	$1.85 \leq N_{rh} \leq 11.93$	$4.21 \leq N_{rh} \leq 24.16$	$10.86 \leq N_{rh} \leq 41.22$	not consistent
$n = 4$	$0.404 \leq \beta < 1$	$N \leq 5.843$	$N \leq 11.45$	$N \leq 22.74$	$N \leq 10.41$
$n = 2$	$0.326 \leq \beta \leq 0.986$	$9.03 \leq \log_{10} \left( \frac{T_{rh}}{GeV} \right) \leq 15.34$	$5.41 \leq \log_{10} \left( \frac{T_{rh}}{GeV} \right) \leq 13.27$	$0.121 \leq \log_{10} \left( \frac{T_{rh}}{GeV} \right) \leq 11.02$	not consistent
$n = 4$	$0.404 \leq \beta < 1$	$\log_{10} \left( \frac{T_{rh}}{GeV} \right) \geq 12.01$	$\log_{10} \left( \frac{T_{rh}}{GeV} \right) \geq 7.868$	$\log_{10} \left( \frac{T_{rh}}{GeV} \right) \geq 0.442$	$\log_{10} \left( \frac{T_{rh}}{GeV} \right) \geq 2.183$

analysis shows that, in this model, it is possible to have a viable reheating phase. In the simple single field inflation with  $\phi^2$  potential, by increasing of  $N_{rh}$ , the effective equation of state parameter changes from  $-1$  and reaches  $\frac{1}{3}$  which is corresponding to a radiation-dominated era.

- Considering the GB effect with  $e^{-\lambda\phi}$  coupling causes the inflation models with both  $\phi^2$  and  $\phi^4$  potentials, in some ranges of the model's parameters, become consistent with the base data at 95% CL. In this case, have studied the model with  $N = 50$ ,  $\lambda = 10$ ,  $\lambda = 10^2$  and  $\lambda = 10^4$  for both  $r - n_s$  and  $r - n_T$  trajectories. When we consider  $n = 2$  and  $\lambda \lesssim 10^2$ , we find the constraint  $0.020 \leq \beta \leq 0.072$  which leads to observational viability of both  $r - n_s$  and  $r - n_T$  trajectories. However, this constraint is not valid for  $n = 2$  and  $\lambda > 10^2$ . By considering for  $n = 4$ , we have  $0.670 \leq \beta \leq 0.716$ . Studying the reheating phase for both cases with  $n = 2$  and  $n = 4$  shows that in these cases also, the effective equation of state parameter changes from  $-1$  and reaches  $\frac{1}{3}$ , which is corresponding to a radiation-dominated era.
- Adding the GB effect to the natural inflation models, makes it observationally viable. In this case also, the larger values of  $\beta$  lead to smaller values of the tensor-to-scalar ratio. By exploring both  $r - n_s$  and  $r - n_T$  trajectories for  $f = 4$ ,  $f = 15$ ,  $f = 35$  and  $f = 60$ , we find  $0.525 \leq \beta < 1$ . For the GB natural inflation, analyzing the reheating phase shows that  $\omega_{eff}$  in this epoch increases from  $-1$  to  $\frac{1}{3}$  which is corresponding to a radiation-dominated era. Therefore, this model has capability to explain the reheating process after inflation.
- With both E-model and T-model potentials, the inflation models are observationally viable, specially for pretty small values of  $\alpha$ . When we consider the GB effect, for any values of  $\alpha$ , the larger values of  $\beta$  lead to the smaller values of the tensor-to-scalar ratio. Therefore, the  $\alpha$ -attractor GB inflation model is consistent with the base and base+GW data sets at 95% CL too. For both E-model and T-model potentials, studying both  $r - n_s$  and  $r - n_T$  trajectories gives  $\beta \leq 4.81 \times 10^{-2}$ . In both E-model and T-model cases, it is possible to explain the reheating process. In both cases, the effective equation of state parameter change from  $-1$  to  $\frac{1}{3}$ .

- Tachyon inflation with  $\phi^2$  potential is consistent with base data just for  $N < 52.7$ . By considering the GB effect, this model would be consistent with observational data for  $N < 62.4$ . Tachyon model with  $\phi^4$  potential is not consistent with the base and base+GW data sets at all. In this case also, the GB effect causes the model becomes observationally viable, for the considered range of  $N$  as  $50 \leq N \leq 70$ . In both cases, the viability arises because the GB effect makes the tensor-to-scalar ratio of the model smaller. Exploring both  $r - n_s$  and  $r - n_T$  trajectories gives  $0.254 \leq \beta < 1$  for  $n = 2$  and  $0.188 \leq \beta < 1$  for  $n = 4$ . By studying the reheating phase in the tachyon model with  $\phi^2$  and  $\phi^4$  potentials, we have found that the reheating epoch cannot be explained in these models. This is because, in these models the effective equation of state parameter doesn't reach  $\frac{1}{3}$  in an observationally viable range of the scalar spectral index.
- Considering the GB effect with  $e^{-\lambda\phi}$  coupling in the tachyon model leads to observationally viable tachyon model with both  $\phi^2$  and  $\phi^4$  potentials. In this case, for smaller values of  $\lambda$  and larger values of  $\beta$ , we have smaller values of tensor-to-scalar ratio which is consistent with the base and base+GW data. This model with  $n = 2$ , for  $N = 50$ ,  $\lambda = 10$ ,  $\lambda = 10^2$  and  $\lambda = 10^4$  for all values of  $\beta$  is observationally viable. For  $n = 4$ , and with  $N = 50$ ,  $\lambda = 10$ ,  $\lambda = 10^2$  and  $\lambda = 10^4$ , we have found  $0.046 \leq \beta$ . We have studied the reheating phase in the tachyon model with dilaton-like GB effect and found that in this case the effective equation of state parameter reaches  $\frac{1}{3}$ . This means that, this model has capability to explain the reheating epoch.
- DBI inflation with  $\phi^2$  and  $\phi^4$  potentials is not consistent with the base and base+GW data sets. However, considering the GB effect with  $\phi^{-2}$  and  $\phi^{-4}$  coupling functions makes the model observationally viable. Note that, the DBI model with  $\phi^2$  potential and  $\phi^{-2}$  GB coupling, in some ranges of the model's parameters is consistent with observational data if  $N \geq 53.1$ . Also, the DBI model with  $\phi^4$  potential and  $\phi^{-4}$  GB coupling, in some ranges of the model's parameters is consistent with observation if  $N \geq 59.6$ . Here also, we have studied the cases with  $N = 50$ ,  $N = 60$  and  $N = 70$  for both  $r - n_s$  and  $r - n_T$  trajectories. The constraints obtained from these studied cases are as  $0.613 \leq \beta \leq 0.948$  for  $n = 2$  and  $0.683 \leq \beta \leq 0.915$  for  $n = 4$ . Analyzing the reheating phase shows that, in this case, we can not get the viable reheating process. In fact, with both potentials the effective equation of state parameter doesn't reach  $\frac{1}{3}$ . Also, with  $\phi^4$  potential, this parameter starts with positive values which is not the case.
- Considering the GB effect with  $e^{-\lambda\phi}$  coupling for the DBI model also, leads to the observational viability of the model with both  $\phi^2$  and  $\phi^4$  potentials. As the previous cases, the GB effects gives the smaller tensor-to-scalar ratio which is consistent with the different data sets. By exploring both  $r - n_s$  and  $r - n_T$  trajectories for  $f = 4$ ,  $f = 15$ ,  $f = 35$  and  $f = 60$ , we have found  $0.332 \leq \beta \leq 0.986$  for  $n = 2$  and  $0.683 \leq \beta \leq 0.948$  for  $n = 4$ . The DBI model with  $\phi^2$  potential and dilaton-like GB coupling loses its viability when we study the reheating phase. This is because the effective equation of state parameter in this case, doesn't reach  $\frac{1}{3}$ . However, the DBI model with  $\phi^4$  potential and dilaton-like GB coupling has capability to explain the reheating phase.

### Acknowledgement

We thank the referee for the very insightful comments that have improved the quality of the paper

considerably. This work has been supported financially by Research Institute for Astronomy & Astrophysics of Maragha (RIAAM) under research project number 1/6025-8.

## References

- [1] Guth, A. 1981, Phys. Rev. D, **23**, 347.
- [2] Linde, A. D. 1982, Phys. Lett. B, **108**, 389.
- [3] Albrecht A., & Steinhard, P. 1982, Phys. Rev. D, **48**, 1220.
- [4] Linde, A. D. 1990, *Particle Physics and Inflationary Cosmology* (Harwood Academic Publishers, Chur, Switzerland).
- [5] Liddle, A. & Lyth, D. 2000, *Cosmological Inflation and Large-Scale Structure*, (Cambridge University Press).
- [6] Lidsey, J. E. et al. 1997, Abney, Rev. Mod. Phys., **69**, 373.
- [7] Riotto, A. 2002, [arXiv:hep-ph/0210162].
- [8] Lyth, D. H. & Liddle, A. R. 2009, *The Primordial Density Perturbation* (Cambridge University Press).
- [9] Maldacena, J. M. 2003, JHEP, **0305**, 013.
- [10] Bartolo, N., Komatsu, E., Matarrese, S. & Riotto, A. 2004 Phys. Rept., **402**, 103.
- [11] Chen, X.2010, Adv. Astron., **2010**, 638979.
- [12] De Felice, A. & Tsujikawa, S. 2011, Phys. Rev. D, **84**, 083504.
- [13] De Felice, A. & Tsujikawa, S. 2011, JCAP, **1104**, 029.
- [14] Nozari, K. & Rashidi, N. 2013, Phys. Rev. D, **88**, 023519.
- [15] Nozari, K. & Rashidi, N. 2016, Advances in High Energy Physics, <https://doi.org/10.1155/2016/1252689>.
- [16] Nojiri, S. & Odintsov, S. D, 2011, Phys. Rept. **505**, 59-144.
- [17] Nojiri, S., Odintsov, S.D. & Oikonomou, V.K., Phys.Rept. 2017, **692**, 1-104.
- [18] Burgess, C.P. 2004, Living Reviews in Relativity, **7**, 5.
- [19] Gross, D.J. & Sloan, J.H. 1987, Nucl. Phys. B, **291**, 41.
- [20] Lovelock, D. 1971, J. Math. Phys., **12**, 498.
- [21] Zwiebach, B. 1985, Phys. Lett. B, **156**, 315.



- [22] Boulware, D. G., & Deser, S. 1985, PRL, **55**, 2656.
- [23] Brown, R. A. 2007, *Brane world cosmology with Gauss-Bonnet and induced gravity terms*, (PhD Thesis), [arXiv:gr-qc/0701083].
- [24] Bamba, K., Guo, Z. K. & Ohta, N. 2007, Prog. Theor. Phys., **118**, 879.
- [25] Andrew, K., Bolen, B. & Middleton, C. A. 2007, Gen. Rel. Grav., **39**, 2061.
- [26] Nozari, K. & Fazlpour, B. 2008, JCAP, **0806**, 032.
- [27] Nozari, K. & Rashidi, N. 2009, Int. J. Thoer. Phys., **48**, 2800.
- [28] Nozari, K. & Rashidi, N. 2009, JCAP, **0909**, 014.
- [29] Nozari, K. & Rashidi, N. 2009, Int. J. Mod. Phys. D, **19**, 219.
- [30] Nojiri, S., Odintsov, S. D., & Sasaki, M. 2005, PRD, **71**, 123509.
- [31] Nojiri, S., & Odintsov, S. D. 2005, Phys. Lett B., **631**, 1.
- [32] Nojiri, S., Odintsov, S. D., & Tretyakov, P. V. 2007, Phys. Lett. B, **651**, 224.
- [33] Guo, Z. K. & Schwarz, D. J., 2009, Phys. Rev. D, **80**, 063523.
- [34] Guo, Z. K. & Schwarz, D. J., 2010, Phys. Rev. D, **81**, 123520.
- [35] Koh, S., Lee, B.-H., Lee, W., & Tumurtushaa, G., 2014, Phys. Rev. D, **90**, 063527.
- [36] Koh, S., Lee, B.-H., & Tumurtushaa, G., 2017, Phys. Rev. D, **95**, 123509.
- [37] Wu, Q., Zhu, T., & Wang, A. 2018, Phys. Rev. D, **97**, 103502.
- [38] Elizalde, E., Odintsov, S.D., Pozdeeva, E.O., & Vernov, S.Yu. 2018, [arXiv:1805.10810].
- [39] Odintsov, S.D., & Oikonomou, V.K. 2018, [arXiv:1808.05045].
- [40] Odintsov, S.D., Oikonomou, V.K., & Banerjee, S. 2018, [arXiv:1807.00335].
- [41] Nojiri, S., Odintsov, S.D., Oikonomou, V.K., Chatzarakis, N. & Paul, T., [arXiv:1907.00403 [gr-qc]].
- [42] Jiang, P.-X., Hu, J.-W., & Guo, Z.-K. 2013, Phys. Rev. D, **88**, 123508.
- [43] Komatsu, E., et al. 2009, Astrophys. J. Suppl., **180**, 330.
- [44] Ade, P. A. R., et al. 2014, Astron. Astrophys., **571**, A22.
- [45] Ade, P. A. R., et al. 2014, Phys. Rev. Lett., **112**, 241101.
- [46] Ade, P. A. R., et al. 2016, Phys. Rev. Lett., **116**, 031302.
- [47] Kaiser, D. I., & Sfakianakis, E. I., 2014, Phys. Rev. L, **112**, 011302.

- [48] Ferrara, S., Kallosh, R., Linde, A., & Porrati, M. 2013, Phys. Rev. D, **88**, 085038.
- [49] Kallosh, R., Linde, A., & Roest, D. 2013, JHEP, **1311**, 198.
- [50] Kallosh, R., Linde, A., & Roest, D. 2014, JHEP4 **1408**, 052.
- [51] Cecotti, S., & Kallosh, R. 2014, JHEP, **05**, 114.
- [52] Kallosh, R., Linde, A., & Roest, D. 2014, JHEP, **09**, 062.
- [53] Linde, A., JCAP, **05**, 003.
- [54] Joseph, J., Carrasco, M., Kallosh, R., & Linde, A. 2015, Phys. Rev. D, **92**, 063519.
- [55] Joseph, J., Carrasco, M., Kallosh, R., & Linde, A. 2015, JHEP, **10**, 147.
- [56] Kallosh, R., Linde, A., Roest, D., & Wrase, T. 2016, JCAP, **1611**, 046.
- [57] Shahalam, M., Myrzakulov, R., Myrzakul, S., & Wang, A. 2016, [arXiv:1611.06315 [astro-ph.CO]].
- [58] Odintsov, S. D., & Oikonomou, V. K. 2016, Phys. Rev. D, **94**, 124026.
- [59] Rashidi, N., & Nozari, K. 2018, Int. J. Mod. Phys. D, **27**, 1850076.
- [60] Nozari, K., & Rashidi, N. 2018, The Astrophysical Journal, **863**, 133.
- [61] Nozari, K., & Rashidi, N. 2017, Phys. Rev. D, **95**, 123518.
- [62] Yi, Z., Gong, Y., & Sabir, M. 2018, [arXiv:1804.09116].
- [63] Silverstein, E., & Tong, D. 2004, Phys. Rev. D, **70**, 103505.
- [64] Alishahiha, M., Silverstein, E., & Tong, D. 2004, Phys. Rev. D, **70**, 123505.
- [65] Sen, A. 1999, J. High Energy Phys., **10**, 008.
- [66] Sen, A. 2002a, J. High Energy Phys., **07**, 065.
- [67] Sen, A. 2002b, Mod. Phys. Lett. A, **17**, 1797.
- [68] Cardenas, V. H. 2006, Phys. Rev. D, **73**, 103512.
- [69] Spalinski, M. 2007, JCAP, **0705**, 017.
- [70] Deshamukhya, A. & Panda, S. 2009, Int. J. Mod. Phys. D, **18**, 2093.
- [71] Campo, S. d., Herrera, R.n, & Toloza, A. 2009, Phys. Rev. D, **79**, 083507.
- [72] Mizuno, S., & Koyama, K. 2010, Phys. Rev. D, **82**, 103518.
- [73] Nozari, K., & Rashidi, N. 2013, Phys. Rev. D, **88**, 084040.
- [74] Rashidi, N., Nozari, K., & GrØn, Ø. 2018, JCAP, **05**, 044.

- [75] Nozari, K., & Rashidi, N. 2019, The Astrophysical Journal, **882**, 78.
- [76] De Felice, A., & Tsujikawa, S., JCAP, **1104**, 029.
- [77] Nozari, K., & Rashidi, N. 2016, Phys. Rev. D, **93**, 124022.
- [78] Akrami, Y., et al. 2018, [arXiv:1807.06211].
- [79] Akrami, Y., et al. 2018, [arXiv:1807.06209].
- [80] Abbott, L. F., Farhi, E., & Wise, M. B. 1982, Phys. Lett. B, **117**, 29.
- [81] Dolgov, A. D., & Linde, A. D. 1982, Phys. Lett. B, **116**, 329.
- [82] Albrecht, A. J., Steinhardt, P. J., Turner, M. S., & Wilczek, F. 1982 PRL, **48**, 1437.
- [83] Kofman, L., Linde, A. D., & Starobinsky, A. A. 1994, PRL, **73**, 3195.
- [84] Traschen, J. H., & Brandenberger, R. H. 1990, Phys. Rev. D, **42**, 2491.
- [85] Kofman, L., Linde, A. D., & Starobinsky, A. A. 1997, Phys. Rev. D, **56**, 3258.
- [86] Greene, B. R., Prokopec, T., & Roos, T. G. 1997, Phys. Rev. D, **56**, 6484.
- [87] Shuhmaher, N., & Brandenberger, R. 2006, Phys. Rev. D, **73**, 043519.
- [88] Dufaux, J. F., Felder, G. N., Kofman, L., Peloso, M., & Podolsky, D. 2006, JCAP, **0607**, 006.
- [89] Abolhasani, A. A., Firouzjahi, H., & Sheikh-Jabbari, M. 2010, Phys. Rev. D, **81**, 043524.
- [90] Felder, G. N., Garcia-Bellido, J., Greene, P. B., Kofman, L., & Linde, A. D., 2001, PRL **87**, 011601.
- [91] Felder, G. N., Kofman, L., & Linde, A. D. 2001, Phys. Rev. D, **64**, 123517.
- [92] Felder, G. N., Kofman, L., & Linde, A. D. 1999, Phys. Rev. D, **59**, 123523.
- [93] Dai, L., Kamionkowski, M., & Wang, J. 2014, PRL, **113**, 041302.
- [94] Munoz, J. B., & Kamionkowski, M. 2015. Phys. Rev. D, **91**, 043521.
- [95] Cook, J. L., Dimastrogiovanni, E., Easson, D., & Krauss, L. M. 2015, JCAP, **04**, 047.
- [96] Cai, R.-G., Guo, Z.-K., & Wang, S.-J. 2015, Phys. Rev. D, **92**, 063506.
- [97] Ueno, Y., & Yamamoto, K. 2016, Phys. Rev. D, **93**, 083524.
- [98] Bruck, C. v. d., & Longden, C. 2016, Phys. Rev. D, **93**, 063519.
- [99] Mukhanov, V. F., Feldman, H. A., & Brandenberger, R. H. 1992, Phys. Rept., **215**, 203.
- [100] Baumann, D. 2009, [arXiv:0907.5424][hep-th].

- [101] Adams, F.C., Freese, K., & Guth, A.H. 1991, Phys. Rev. D, **43**, 965.
- [102] Freese, K., Frieman, J.A., & Olinto, A.V. 1990, Phys. Rev. Lett., **65**, 3233.
- [103] Freese, K., & Kinney, W.H. 2004, Phys. Rev. D, **70**, 083512.
- [104] Kallosh, R., & Linde, A. 2013, J. Cosmol. Astropart. Phys., **1307**, 002.
- [105] Kallosh, R., & Linde, A. 2013, J. Cosmol. Astropart. Phys., **1312**, 006.
- [106] Sami, M., Chingangbam, P., & Qureshi, T. 2002, Phys. Rev. D, **66**, 043530.
- [107] Feinstein, A. 2002, Phys. Rev. D, **66**, 063511.
- [108] Nozari, K., & Rashidi, N. 2014, Phys. Rev. D, **90**, 043522.
- [109] Padmanabhan, T. 2002, Phys. Rev. D, **66**, 021301.
- [110] Gorini, V., Kamenshchik, A.Y., Moschella, U., & Pasquier, V. 2004, Phys. Rev. D, **69**, 123512.
- [111] Copeland, E. J., Garousi, M. R., Sami, M., & Tsujikawa, S. 2005, Phys. Rev. D, **71**, 043003.
- [112] Kofman, L., 1996, [arXiv:astro-ph/9605155].
- [113] Giudice, G. F., Tkachev, I., & Riotto, A. 1999, JHEP, **9908**, 009.
- [114] Wallisch, B. 2018, *Cosmological Probes of Light Relics*, (PhD Thesis), [arXiv:1810.02800 [astro-ph.CO]].
- [115] Dine, M., & Kusenko, A. 2004 , Rev. Mod. Phys, **76**, 1.
- [116] Lozanov, K. D., & Amin, M. A. 2014 , Phys. Rev. D, **90**, 083528.